



Microstructure and High-Temperature Tribological Properties of Nickel-Based Composite Coatings with Laser In Situ Induced TiC and MoSi₂ Reinforcement

Silong Cao^{1,2} · Pu Zhang¹ · Shuai Feng¹ · Jiansong Zhou³

Submitted: 25 August 2023 / in revised form: 4 January 2024 / Accepted: 5 January 2024 / Published online: 28 February 2024
© ASM International 2024

Abstract In order to improve the tribological properties of Inconel 718 alloy at elevated temperature, nickel-based composite coatings with in situ TiC and MoSi₂ reinforcement were deposited onto Inconel 718 alloy via laser cladding the complex Hastelloy C276 alloy and Ti₃SiC₂ powder in this study. The influences of the in situ TiC and MoSi₂ reinforcement from the complete decomposition of Ti₃SiC₂ powders on the microstructure, mechanical and tribological properties of prepared coatings were systematically investigated. These coatings exhibited a microstructure consisting of coarse γ -Ni dendrites, slender interdendritic MoSi₂ phases, and TiC ellipsoidal particles. The inclusion of an appropriate amount of in situ fine TiC and MoSi₂ precipitates significantly inhibited the directional growth and coarsening of γ -Ni dendrites, resulting in improved mechanical properties and wear resistance. Among the three types of coatings applied through laser cladding, the Ni-based composite coating with 20 wt.% Ti₃SiC₂ addition demonstrated relatively high hardness (538.4 HV_{0.3}) and flexural strength (1651.37 MPa),

coupled with a lower mean friction coefficient (0.39) and wear rate (3.16×10^{-5} mm³/N m) at 30 °C. These TiC and MoSi₂ reinforcements proved effective in reducing cutting stress and resisting plastic deformation, thereby enhancing friction coefficients and wear rates across the temperature range from 30 to 400 °C. The prepared coatings also exhibited promising wear resistance at 800 °C, attributed to the formation of protective tribofilm oxidative layers. However, the breakage of the lubricating tribofilms caused obvious wear damage and exacerbated friction coefficients and wear rates at 1000 °C.

Keywords Laser in situ synthesis · Ni-based wear resistant coating · Mechanical properties · High-temperature wear mechanism

Introduction

Nickel-based superalloys are an extremely important and functional set of materials widely employed in the military, aerospace, rocket engine, and gas turbine manufacturing industries because of their excellent mechanical properties, corrosion and oxidative resistance, and stable solid solution ability at high temperatures [1–3]. Hastelloy C276 alloy, a representative superalloy, readily forms a simple γ -Ni austenitic solid solution which improves the microstructural stability of this alloy at elevated temperatures. Additionally, Hastelloy C276 alloy demonstrates excellent corrosion resistance across various corrosive media and achieves higher microhardness after heat treatment at 800 °C, rendering it suitable for extreme high-temperature applications (>800 °C) [4, 5]. However, as industrial applications advance and the demand for cutting-edge systems grows, superalloy-based components must

✉ Silong Cao
slcao@imut.edu.cn

✉ Jiansong Zhou
jszhou@licp.cas.cn

¹ School of Materials Science and Engineering, Inner Mongolia University of Technology, Hohhot 010051, People's Republic of China

² Engineering Research Center of Development and Processing Protection of Advanced Light Metals, Ministry of Education, Hohhot 010051, People's Republic of China

³ Key Laboratory of Science and Technology on Wear and Protection of Materials, Lanzhou Institute of Chemical Physics, CAS, Chinese Academy of Sciences, Lanzhou 730000, People's Republic of China

withstand significant temperature fluctuations and harsh engineering environments [6]. Under such conditions, superalloys often experience severe oxidation and wear damage, resulting in overall surface failure. Surface failure severely compromises the operational safety of these components. Surface coating technology can effectively restore the damaged region and provide a feasible way to regenerate the comprehensive properties of nickel-based superalloys, owing to the advantages of this approach, such as low preparation cost, flexible application scenarios, different chemical composition and structure to the substrate [7–9]. Moreover, since both wear and oxidation typically initiate at the component's surface, the economic and technological advantages of designing and producing wear- and oxidation-resistant coatings capable of functioning across a wide temperature range for nickel-based superalloy components have become evident [10, 11].

Drawing on the unique wear resistance mechanism of ceramic-based composites, numerous researchers have found that the introduction of ceramic particles into materials could effectively suppress plastic deformation and impart excellent tribological properties at elevated temperatures [12, 13]. Consequently, to enhance mechanical properties and wear resistance at high temperatures, nickel-based composites with high-volume-fraction ceramic reinforcements have been developed [14, 15]. These reinforcing materials, such as $\text{Bi}_2\text{O}_3/\text{TiO}_2$ [16], TiB_2 [17], TiC [18], SiC [19], Cr_3C_2 [20], among others, were commonly utilized to strengthen the alloy matrix due to their high strength and elastic moduli at elevated temperature. In addition, the role of TiC ceramic particles in the nickel-based composite coatings has been reported in previous studies [21]. MoSi_2 ceramic has been considered a competitive reinforcement to protect the heating components at elevated operating temperature because of its high strength and microhardness at temperature of up to 1450 °C [22]. Furthermore, TiC exhibited good interfacial compatibility with MoSi_2 due to the similarity in their thermal expansion coefficients (TiC $7.4 \times 10^{-6} \text{ K}^{-1}$, MoSi_2 $5.1 \times 10^{-6} \text{ K}^{-1}$) [23–25]. The conjoint direct addition of TiC and MoSi_2 reinforcements significantly improved the hardness and fracture toughness, wear and oxidation resistance for the plastic alloy matrix in ambient and elevated temperature. However, although the γ -Ni solid solution has excellent wettability with many ceramic hard particles to effectively eliminate the inherent defects and to acquire high quality interfacial binding strength, the preparation of composites by direct addition of ceramic particles is more prone to these problems of component aggregation, and grain coarsening of the TiC and MoSi_2 phases compared with the in situ synthesis method [26–28]. Furtherly, Liu et al. reported that the laser in situ synthesized synthesis of Cr_7C_3 , TiC , and TiB particles could substantially enhance

the mechanical and tribological properties of Nickel-based alloys via the complex Ni60 alloy and Ti_3SiC_2 powder as the raw materials. These laser in situ Cr_7C_3 , TiC , and TiB particles were mainly originated by the complete decomposition and further reactions of Ti_3SiC_2 powders under the action of the high-energy laser beam. At the same time, laser in situ synthesized ceramic particles presented fine grain size and uniform distribution in the γ -Ni matrix and generated grain refinement and dispersion strengthening effects of the Ni60- Ti_3SiC_2 composite coatings [29]. In recent years, numerous nickel-based composites with outstanding tribological properties were prepared and applied in the aerospace industry. Nevertheless, most experimental studies on the high-temperature performance of crucial engineering nickel-based lubricating composites have been limited to temperature below 800 °C [30, 31]. Consequently, it holds significant practical importance to explore the wear resistance of lubricating materials and develop a novel Ni-based composite that exhibits exceptional wear resistance properties at extremely high temperature [32, 33].

This paper presents Ni-based composite coatings with laser in situ induced TiC and MoSi_2 reinforcements, utilizing the complex Hastelloy C276 alloy and different amounts of Ti_3SiC_2 powder as the raw materials. We analyzed the effect of in situ synthesized TiC and MoSi_2 reinforcements on the composition, microstructure, mechanical and tribological properties of three deposited composite coatings. The primary objective of this study is to analyze the influence of the formation and breakdown of oxidative tribofilms on the tribological performance of the composite coatings across the temperature range from 30 to 1000 °C, providing a technical reference for the development of a novel nickel-based wear resistant composite at high temperature.

Materials and Methods

Materials and Laser Cladding Procedure

In this study, we selected commercially available Inconel 718 superalloy as the substrate, with dimensions of Φ 50 mm \times 10 mm. The chemical compositions of the Inconel 718 superalloy, the Hastelloy C276 powder, and the Ti_3SiC_2 powder are listed in Table 1. The Hastelloy C276 and Ti_3SiC_2 powders were procured from the Höganäs company. We blended three types of feedstock powders, each with varying Ti_3SiC_2 weight ratios (10NT, 20NT, and 30NT, corresponding to 10%, 20%, and 30% wt. Ti_3SiC_2 in Hastelloy C276), using a vario-planetary high-energy ball milling process. The mill operated at a relative rotary speed of 200 rev/min for 8 h. In order to

Table 1 Chemical compositions and particle size of Inconel 718 superalloy, Hastelloy C276 powder, and Ti₃SiC₂ powder.

Powder	Composition (wt.%)	Particle size (μm)
Inconel 718	50.0–55.0% Ni, 17.0–21.0% Cr, 2.8–3.3% Mo, 0.65–1.15% Ti, 0.2–0.8% Al, 0.08% C, balance Fe	/
Hastelloy C276	56.26% Ni; 16.20% Mo; 16.67% Cr; 6.55% Fe; 2.66% W; 0.8% Mn; impurities < 0.86%	60
Ti ₃ SiC ₂	Impurities < 1%	5–10

ensure the uniform dispersion of the mixed powders, hard tungsten carbide balls were used as mixing balls with the ball-to-powder mass ratio of 20:1.

Composite coatings were prepared using a CW fiber laser processing system (IPG-YLS-4000, Germany) with a maximum power of 4000 W and a wavelength of 1064 nm. After conducting numerous experiments, we determined the suitable processing parameters: laser power of 1.7 kW, scanning velocity of 1000 mm/min, overlapping ratio of 50%, spot diameter of 4 mm, and preset powder thickness of 2 mm. We used argon as the shielding gas. The production of single-pass samples employed the same processing parameters as the production of full coatings. The prepared coatings were polished using silicon carbide waterproof abrasive papers with mesh sizes of 120, 600, 1000, 1500, and 2000. Subsequently, they were burnished with water-soluble diamond grinding paste until the surface Ra reached 0.05 μm, ensuring suitability for subsequent characterization and testing. We examined the Ra of the burnished samples using a confocal optical microscope (MicroXAM-800).

Composition and Microstructure

We identified the phase composition of the raw powder and the coating surfaces using X-ray diffraction (XRD, D/MAX-2400 Rigaku, Japan) with Cu K α irradiation (wavelength $\lambda = 0.1540598$ nm), scanning in the range of $2\theta = 20\text{--}80^\circ$ at a scanning rate of $5^\circ/\text{min}$. We observed the morphologies, microstructures, and elemental compositions of the post-processed coatings using an optical microscope (OM, AXIO Imager, A2 m) and scanning electron microscopy (SEM, JEOL-JSM-5600LV) equipped with energy-dispersive spectroscopy (EDS). Since our primary focus was to investigate the influence of the phase composition and microstructure of the prepared composite coatings on tribological properties and wear mechanisms, it was essential to characterize the coating surfaces. Electrolytic polishing of the top surface of the 10NT and 20NT composite coatings in a 90% methanol and 10% perchloric acid mixture preceded the application of the electron backscatter diffraction (EBSD) technique via EDAX-TSL

SEM + Oxford instruments EBSD system. EBSD data concerning the phase distribution maps and grain characteristics at top surface of the 10NT and 20NT composite coatings were obtained with an accelerating voltage of 20 kV and a working distance of 20 mm, utilizing the OIM software with the recommended noise reduction.

Mechanical and Tribological Property at Elevated Temperature

We conducted microhardness testing on the cross sections of post-processed coatings using a Vickers microhardness tester (MH-5-VM) with a load of 300 g and a dwell time of 5 s. Surface nanohardness and elastic modulus of post-processed coatings were obtained through nanoindentation characterization using an NHT02–05987 tester (CSM Diamond indenter, Switzerland). We set the maximum load at 8 mN, with a holding load time of 10 s and loading/unloading times of 30 s each. The flexural strength was determined for processed samples with dimensions of $20 \times 3 \times 1.5$ mm³ using an electronic universal material testing machine (CMT5202, Shenzhen Sans Material Test Instrument Co., China) at a nominal cross head speed of 0.1 mm/min and a span of 16 mm. For the preparation of flexural strength test samples, the prepared coating was first peeled off from the substrate bonding interface and then, processed and polished to the final size ($20 \times 3 \times 1.5$ mm³) using wire cutting technology and silicon carbide waterproof abrasive papers. Each mechanical property test was performed on at least three samples and five sets of parallel data to finally determine the average value.

For dry sliding tribology tests of post-processed coatings, we employed a ball-plate rotating sliding configuration testing device (Rtec-3000F, USA). Si₃N₄ balls with a diameter of 6.35 mm and a microhardness of 1700 ± 20 HV were installed on the fixed holder, while the deposited coatings with dimensions of $\Phi 25 \times 5$ mm³ cylinders were placed on the movable bottom holder. The wear test conditions included a sliding speed of 18.8 cm/s, a test period of 60 min, a normal load of 15 N, a rotating radius of 5 mm, and a total sliding distance of 676.8 m. Tests were

conducted at selected temperatures of 30, 200, 400, 800, and 1000 °C. We recorded the friction coefficient using a signal acquisition system. Morphological analysis of the wear track and wear volume was performed using a confocal optical microscope (MicroXAM-800). To minimize experimental error, three repeated wear tests were conducted, and the average values of the friction coefficient and wear rate were reported. The worn surface was characterized using SEM with EDS and a Raman spectrometer (Renishaw inVia, UK, Laser wavelength: 532 nm).

Results and Discussion

Phase Composition and Microstructure

The SEM morphology and elemental distribution of the raw mixed powders after ball milling pretreatment are depicted in Fig. 1. The mixed powder of the 10NT coating mainly consists of ellipsoidal particles with a diameter of approximately 40–60 μm and fine cluster particles. Elemental mapping characterization reveals that the ellipsoidal and cluster particles correspond to Hastelloy C276 alloy and Ti₃SiC₂ ceramic, respectively. During the ball milling process, the Ti₃SiC₂ particles continuously collide and cold weld to the soft C276 alloy, resulting in particle shattering and adherence to the exposed surface of the alloy matrix [34]. With an increased Ti₃SiC₂ particle content, the 20NT

composite coating exhibits an enrichment of fine ceramic particles and a significant increase in oxygen content (Fig. 1b). When the Ti₃SiC₂ particle content is further increased to 30 wt.% in the 30NT composite powder, the exposed surface of the Hastelloy C276 matrix becomes almost entirely covered by ceramic particles, and the extent of fine Ti₃SiC₂ particles increases sharply (Fig. 1c). At the same time, the oxygen content in the mixed 30NT composite powder increases from 1.15 to 3.73 wt.% compared to the 10NT composite powder. In the high-energy ball milling process, the frictional heat accumulation caused by continuous collisions can create conditions for reactions between Ti and O, exacerbating the degree of oxidation of the Ti₃SiC₂ active particles and resulting in a significant increase in oxygen content in the mixed 30NT composite powder [35]. Meanwhile, an excess of Ti₃SiC₂ particles leads to segregation on the surface of the C276 alloy matrix, which is detrimental to achieving composite coatings with a uniform content and microstructure.

The phase compositions of the post-processed coatings produced with various Ti₃SiC₂ reinforcements are presented in Fig. 2. In the 10NT coating, the mixed initial powders mainly consist of γ-Ni solid solution (Cubic, Fm-3 m (230)) and Ti₃SiC₂ (Hexagonal, P63/mmc (194)) ceramic, with no obvious impurity phases detected (Fig. 2a). With the introduction of 20 and 30 wt.% Ti₃SiC₂, the intensities of the Ti₃SiC₂ diffraction peaks increase significantly, and no new identified phases appear,

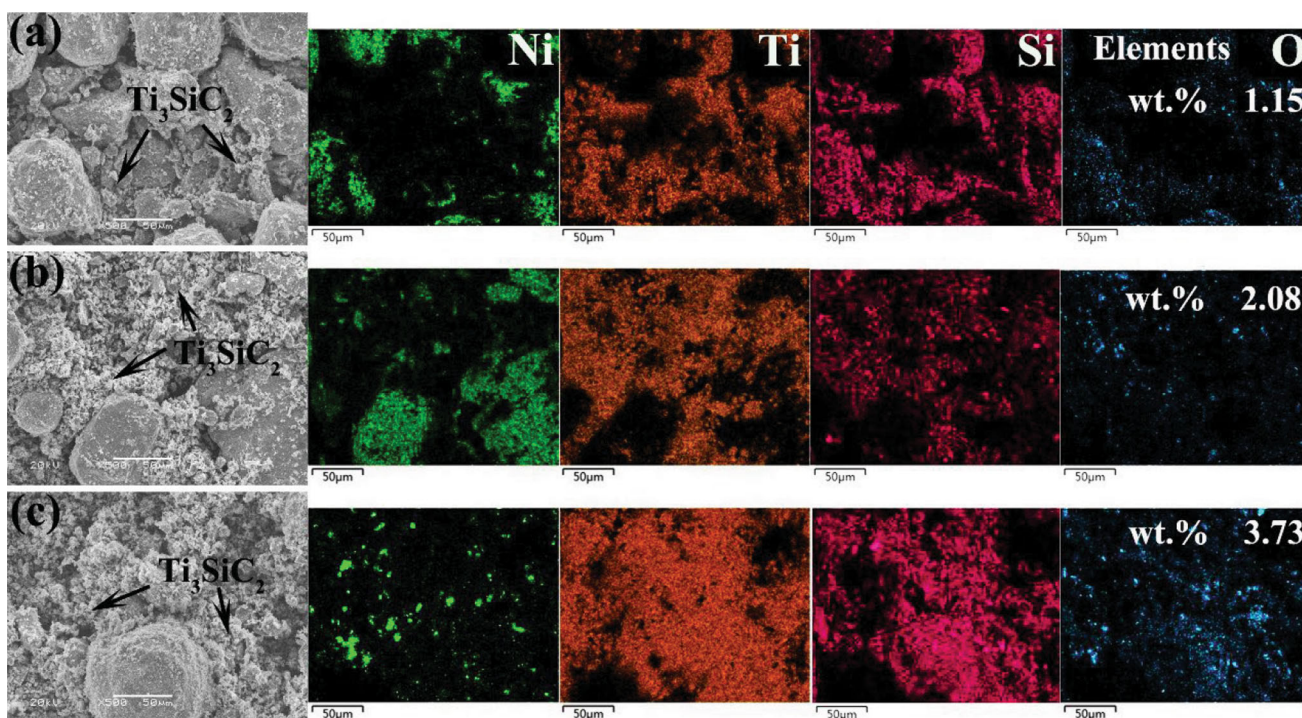


Fig. 1 SEM morphology and elemental mapping of raw powders: (a) 10NT, (b) 20NT, and (c) 30NT.

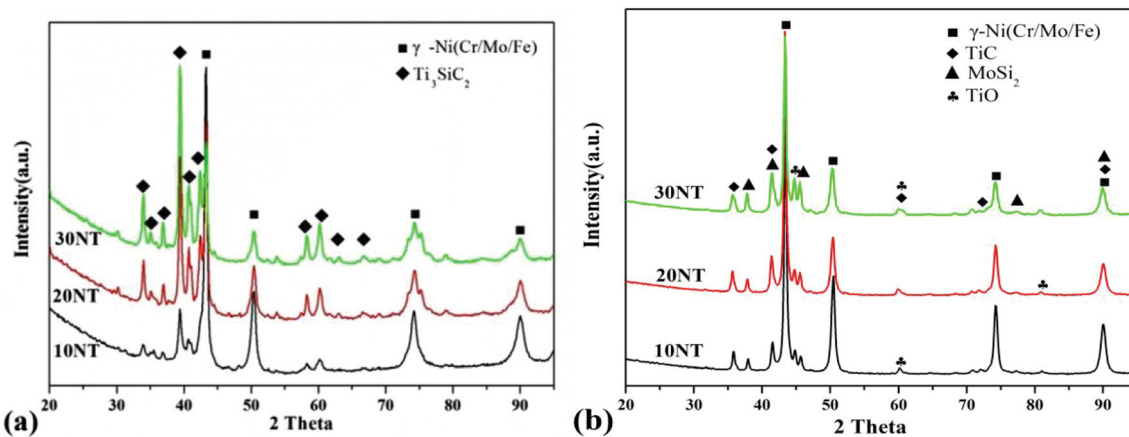
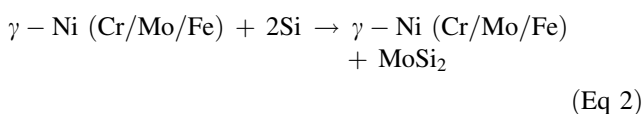
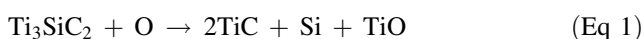


Fig. 2 XRD patterns of the (a) raw powders and (b) composite coatings deposited under various conditions.

indicating that the cladding powders maintain compositional stability during the high-energy ball milling process. Fig. 2b reveals that the 10NT composite coating primarily consists of γ -Ni (Cr/Mo/Fe) solid solution, laser in situ induced TiC (Cubic, Fm-3 m (230)) and MoSi₂ (Tetragonal, I4/mmm (139)) reinforcing phases, along with a small amount of TiO (Cubic, Fm-3 m (230)) ceramic particles. The presence of the TiO phase confirms that the laser cladding process can create the high temperatures and low oxygen partial pressure conditions necessary to generate a minor content of TiO. Notably, there are no diffraction peaks of Ti₃SiC₂ in the laser clad 10NT coating, in contrast to the feedstock, indicating that Ti₃SiC₂ is entirely converted into TiC and free Si due to the complex interactions between the laser beam and the powder. The MoSi₂ reinforcing precipitates are generated by the reaction of free Si with Mo that has escaped from the γ -Ni solid solution due to the relatively negative mixing enthalpy between Mo and Si [36, 37]. Since the XRD analyses are performed under the same conditions, it is presumed that the content of laser in situ induced TiC and MoSi₂ phases in the 20 and 30NT composite coatings is relatively higher than that in the 10NT coating due to the higher diffraction intensity as the Ti₃SiC₂ content is increased. In accordance with prior research, it is well-documented that Ti₃SiC₂ tends to decompose and give rise to fine TiC reinforcement during the laser-based preparation process [10]. In this study, the Ti₃SiC₂ feedstocks undergo complete transformation into TiC and MoSi₂ reinforcements through laser in situ synthesis. The potential transformation process for Ti₃SiC₂-reinforced Ni-based composite coatings produced by laser cladding can be described as follows [11, 35]:



The detailed evolution of the cross-sectional microstructure and EDS results at the upper regions of the three types of post-processed composite coatings is illustrated in Fig. 3. The microstructure of the 10NT composite coating is predominantly composed of coarse acicular columnar dendrites with a noticeable growth orientation, as well as small ellipsoidal particles and interdendritic particles in stripe shape. Based on the XRD results and elemental distribution presented in Fig. 3a, the coarse columnar dendrites and fine interdendritic particles are identified as the γ -Ni solid solution (designated as 1) and laser in situ induced MoSi₂ reinforcing ceramic (designated as 2). The distinct chemical compositions of the spot 1 and spot 2 regions are Ni_{57.87}Cr_{16.02}Mo_{11.02}Fe_{6.83}W_{1.63}Ti_{2.21}Si_{0.91}C_{3.51} and Ni_{15.30}Cr_{5.08}Mo_{49.52}Fe_{3.43}W_{1.36}Ti_{3.23}Si_{18.02}C_{4.06} (wt.%), respectively (Table 2). The fine ellipsoidal particles are confirmed to be TiC ceramic (designated as 3) since this region primarily contains distributed Ti and C elements (chemical composition: Ni_{14.27}Cr_{6.80}Mo_{3.86}Fe_{2.19}W_{1.03}Ti_{54.26}Si_{2.16}C_{15.43}). The in situ TiC reinforcement may form the carbides precipitate due to the direct complete decomposition of Ti₃SiC₂ powders and, as a result, become fine ellipsoidal particles. The formation of MoSi₂ can be attributed to eutectic precipitation from a liquid phase that contains an excess Si from the decomposition of Ti₃SiC₂. This means that, in the case of the 10NT coating, the original feedstocks are inclined to generate a large number of coarse columnar dendrites in the form of γ -Ni solid solution. Furthermore, the laser in situ generated TiC and MoSi₂ reinforcing ceramic particles exhibit a fine grain size and are uniformly dispersed in the γ -Ni dendrite matrix without any noticeable element agglomeration.

Despite its higher Ti₃SiC₂ content, the 20NT composite coating still exhibits characteristic features such as coarse γ -Ni dendrites (designated as 4), slender MoSi₂

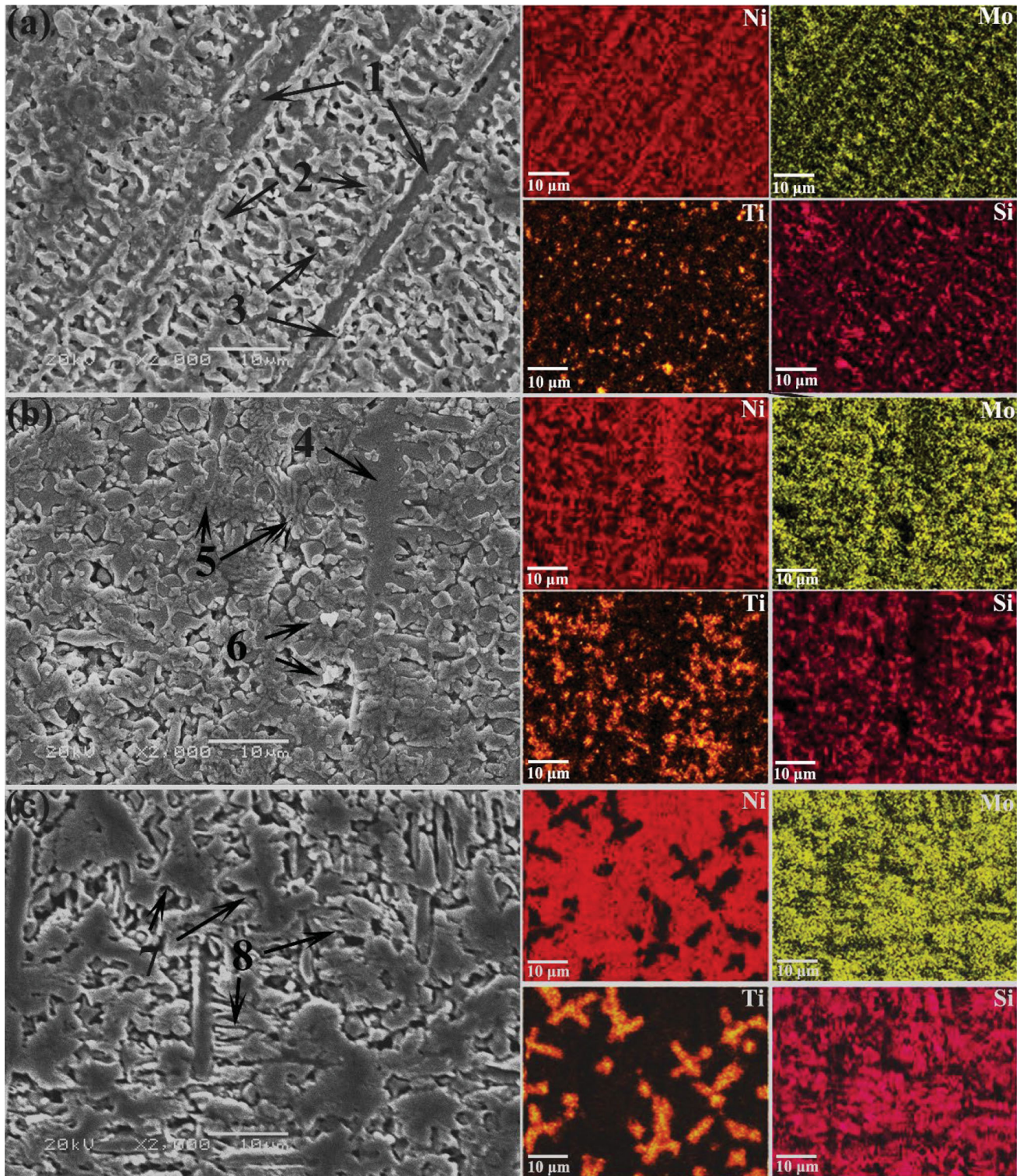


Fig. 3 Sectional SEM and EDS elemental mapping images of the microstructure for composite coatings: (a) 10NT, (b) 20NT, and (c) 30NT.

interdendritic phases (designated as 5), and TiC ellipsoidal particles (designated as 6), as depicted in Fig. 3b. The chemical composition of different grain morphologies in the 20NT composite coating is presented in Table 2. As

indicated by the elemental mapping, the relative Ti and Si content is significantly increased in the 20NT composite coating when compared to the 10NT coating. The higher Ti and Si EDS counts from the interdendritic areas of the

Table 2 Chemical composition in the areas marked in Fig. 3 determined by EDS.

Regions	Composition (wt.%)								Phases
	Ni	Cr	Mo	Fe	W	Ti	Si	C	
1	57.87	16.02	11.02	6.83	1.63	2.21	0.91	3.51	γ -Ni
2	15.30	5.08	49.52	3.43	1.36	3.23	18.02	4.06	MoSi ₂
3	14.27	6.80	3.86	2.19	1.03	54.26	2.16	15.43	TiC
4	55.42	14.75	8.89	5.01	3.07	9.68	0.98	2.21	γ -Ni
5	14.13	3.99	52.81	2.34	1.65	5.08	16.44	4.45	MoSi ₂
6	13.35	6.46	2.89	2.32	1.15	55.17	2.08	16.58	TiC
7	12.95	5.76	2.35	2.61	1.27	56.69	1.86	16.51	TiC
8	12.54	3.67	54.67	2.07	1.35	4.85	16.57	4.28	MoSi ₂

20NT samples correspond with the more intense TiC and MoSi₂ XRD peaks shown in Fig. 2. However, with a further increase in the Ti₃SiC₂ content to 30 wt.% in the 30NT composite coating, distinctive bulky and fan-shaped TiC ceramic particles precipitate (designated as 7), as shown in Fig. 3c. It is worth noting that in the 30NT coating, there is an accumulation of Ti and Si, along with the segregation of Mo from the γ -Ni matrix. This observation suggests that the excess of Ti₃SiC₂ results in a pronounced enrichment of TiC and MoSi₂ reinforcement phases (designated as 8) due to the poor solubility between the γ -Ni matrix and the bulky ceramic phases.

The cross-sectional and magnified optical morphologies of the three composite coatings with varying Ti₃SiC₂ content are presented in Fig. 4. All the composite coatings exhibit a noticeable melt depth, contributing to the formation of a strong metallurgical bond, and the thickness remains relatively consistent even with increased Ti₃SiC₂ content. Apparent defects are hardly discernible in the 10NT and 20NT composite coatings, as shown in Fig. 4a, b. Additionally, all three composite coatings exhibit a dendritic microstructure in the transverse areas of the γ -Ni solid solution due to the rapid cooling and heat conduction between the substrate and molten pool [38]. However, the laser in situ induced TiC and MoSi₂ reinforcing phases display different microstructural morphologies in the various composite coatings. In the 10NT composite coating, the sectional microstructures primarily consist of γ -Ni columnar dendrites, fine TiC, and MoSi₂ interdendritic particles (Fig. 4a). In the case of the 20NT composite coating, the increased content of fine TiC and MoSi₂ interdendritic precipitates hinders and disrupts the growth of γ -Ni columnar dendrites (Fig. 4b). The grain size of the TiC and MoSi₂ interdendritic particles in the 20NT composite coating significantly increases, and the directional growth of the γ -Ni dendrites weakens compared to the 10NT coating. Notably, as shown in Fig. 4c, the 30NT composite coating exhibits distinct microstructural characteristics. It features cracks and pores in its sectional morphology, particularly when the Ti₃SiC₂ content reaches

30 wt.%. Vertical cracks and large pores develop at the top and bottom of the coating region, respectively. The cluster-like fan-shaped TiC ceramic and irregular MoSi₂ grains are unevenly distributed in the γ -Ni matrix in the 30NT composite coating. Uneven ceramic distribution leads to increased trend of crack formation, while the generated pores mainly result from the agglomeration of coarse ceramic particles, creating cavities during the melt cooling [11, 25, 34].

The top surface features of phase mapping and grain morphology of the 10NT and 20NT composite coatings are confirmed through EBSD characterization, as shown in Figs. 5 and 6, respectively. The volume fractions of TiC and MoSi₂ particles in the 10NT coating are 1.8% and 1.4%, respectively, as per Fig. 5a. In the 20NT composite coating, the volume fractions of TiC and MoSi₂ particles increase to 3.7% and 2.4%, respectively, as shown in Fig. 6a. The maximum grain size of the γ -Ni solid solution reaches 82 μ m, and the corresponding frequency of this grain size is 81.5% for the 10NT coating, as displayed in Fig. 5a. Meanwhile, the mean grain size of the fine reinforcing TiC ellipsoidal particles is approximately 3 μ m, while the MoSi₂ interdendritic particles, with a relatively low-volume fraction, are refined to a grain size of 1 μ m. These in situ generated TiC and MoSi₂ particles are uniformly dispersed in the γ -Ni matrix. In the case of the 20NT coating, the mean grain sizes of the γ -Ni dendritic matrix range between 38 and 67 μ m, representing a total grain size frequency of 81.5% (Fig. 6a). It is evident that the TiC ellipsoidal particles and low-volume-fraction MoSi₂ interdendritic particles are coarsened to grain sizes of 5 and 2.5 μ m, respectively, in the 20NT composite coating. In line with the XRD and SEM results, the increased content of in situ synthesized TiC and MoSi₂ reinforcing precipitates helps to inhibit the directional growth and grain growth and finally, generate fine dendrites of the γ -Ni matrix [11, 25]. The prominent preferred orientation and the small-angle grain boundary (<5°) of the γ -Ni matrix in the 10NT composite coating result from the pronounced directional solidification (Fig. 5b) [39].

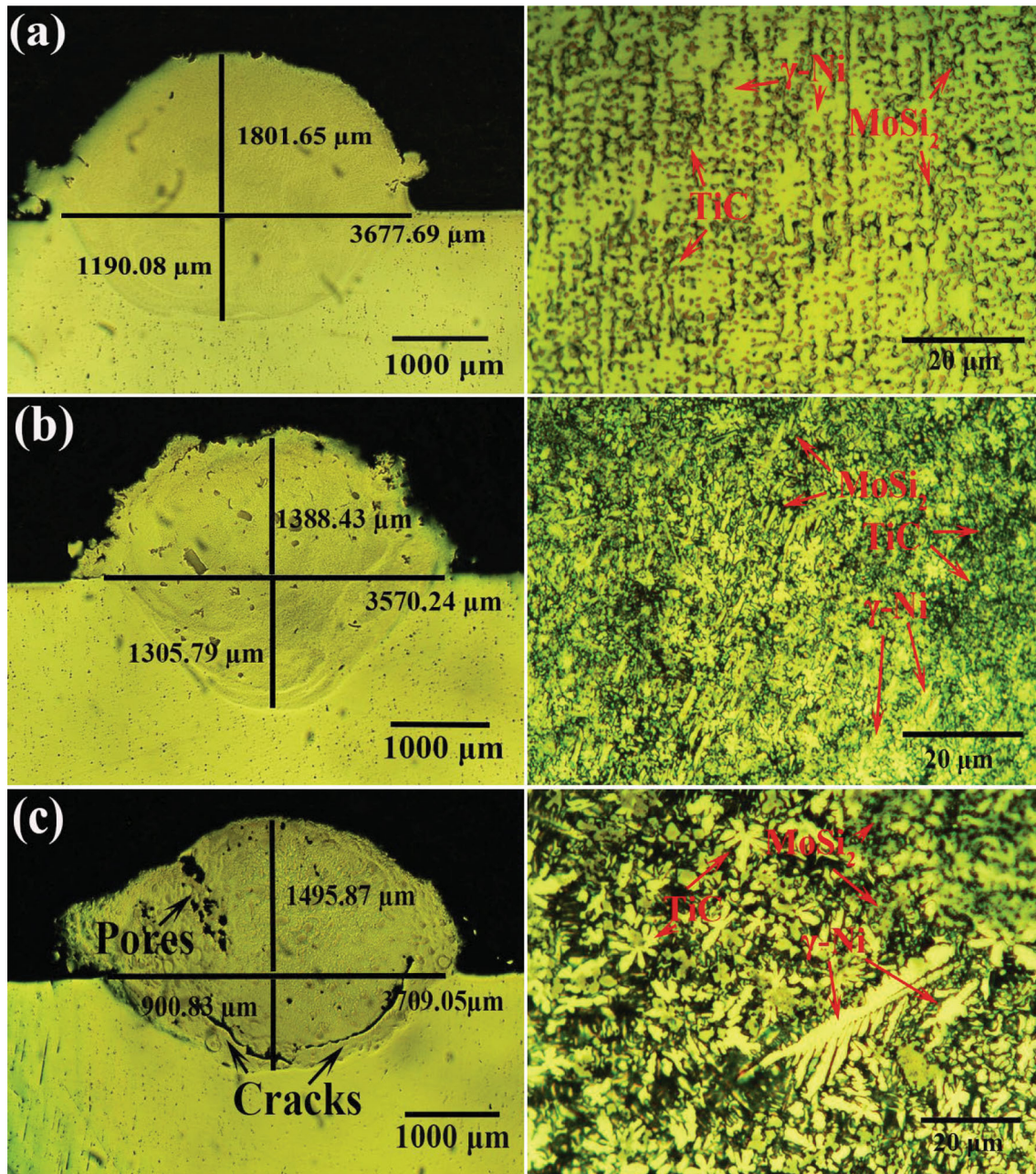


Fig. 4 Typical single-pass sectional morphology and corresponding magnified microstructure: (a) 10NT, (b) 20NT, and (c) 30NT.

Conversely, high-angle grain boundary scattering, ranging from 20 to 60°, is found in the 20NT composite coating due to the poor solubility between the γ -Ni matrix and the bulky TiC and MoSi₂ reinforcement phases. Additionally, it is apparent that the γ -Ni matrix exhibits a significant texture index, particularly in the three pole figures (PFs) of the 10NT composite coating. Notably, there is a maximum texture index of up to 33.9 in the case of the {101} and {111} PFs (Fig. 5c). In the 20NT coating, the volume fraction of small-angle grain boundaries (<5°) significantly decreases from 0.59 to 0.32, indicating a reduced relative

content of the γ -Ni matrix and an increase in synthesized TiC and MoSi₂ ceramic reinforcement (Fig. 6b). The orientation growth of the γ -Ni matrix is inhibited by the in situ TiC and MoSi₂ refinements in the 20NT coating, resulting in a weak texture index for the cubic γ -Ni matrix. The maximum texture index is only 17.7 for all PFs (Fig. 6c).

Microhardness and Flexural Fracture Properties

The transverse microhardness distribution of the prepared Ni-based composite coatings with varying Ti₃SiC₂ content

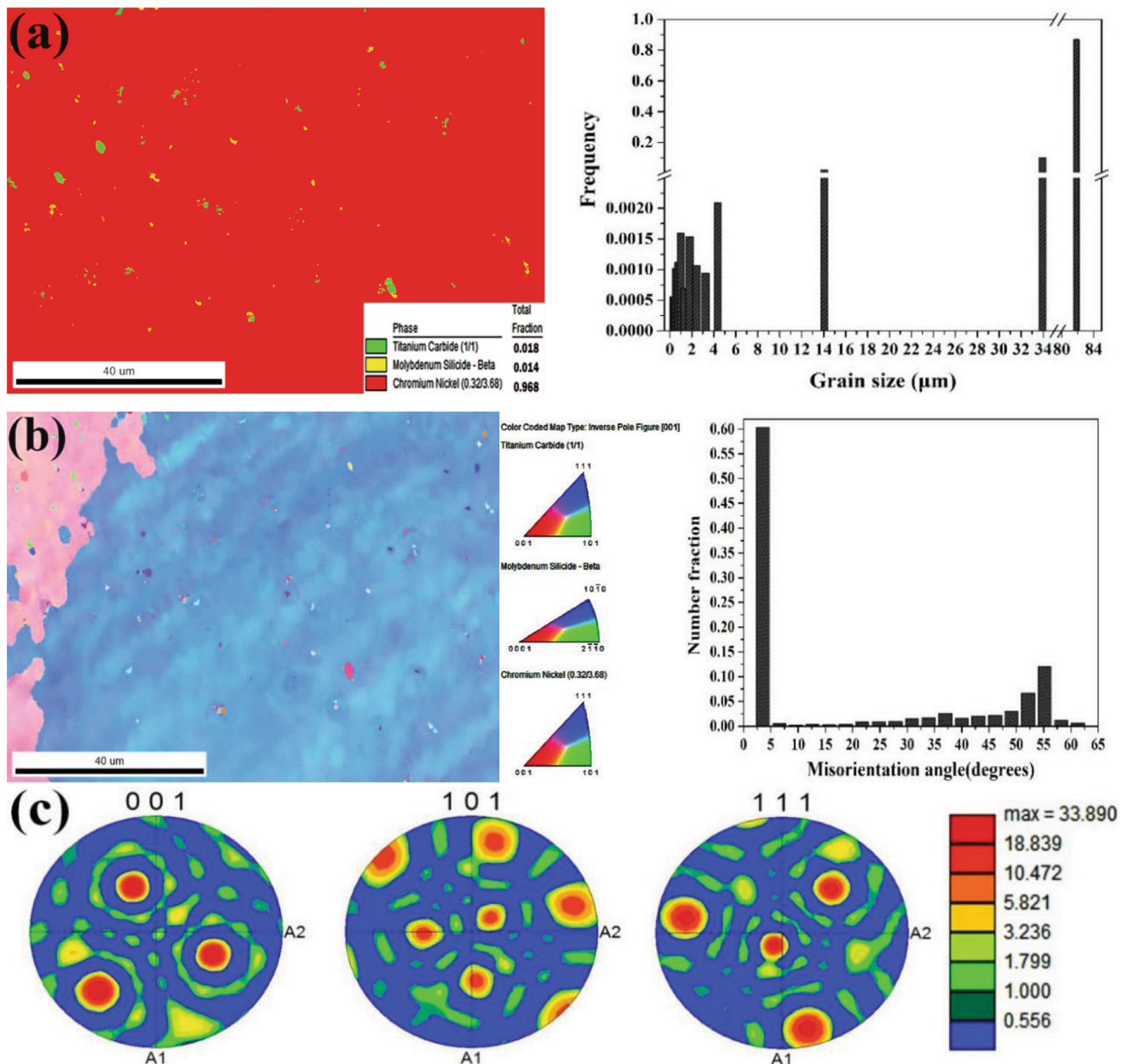


Fig. 5 (a) EBSD phase mapping images (red: γ -Ni, yellow: MoSi₂, green: TiC), (b) EBSD grain IPFs and misorientation angles, and (c) {001}, {101}, and {111} PFs of the γ -Ni matrix in the 10NT composite coating.

is shown in Fig. 7. In the case of the 10NT coating, the mean microhardness values are approximately 445.5 ± 5.3 HV_{0.3} and the values are evenly distributed across the coating thickness, significantly surpassing those of the Inconel 718 substrate (244.6 ± 3.3 HV_{0.3}). The laser in situ generated MoSi₂ and TiC particles primarily contribute to the second-phase strengthening, substantially increasing the microhardness of the 10NT coating. The mean hardness of the 20NT composite coating reaches around 538.4 ± 8.3 HV_{0.3} due to the increased relative fraction of laser in situ generated TiC and MoSi₂ reinforcing particles. Interestingly, the microhardness of the

30NT coating exceeds that of the 20NT coating, measuring approximately 578.6 ± 24.2 HV_{0.3}. However, the hardness values exhibit significant fluctuations at different depths within this coating. It is presumed that the microhardness is influenced by the quantity of fine TiC and MoSi₂ precipitated reinforcement in the three composite coatings. Furthermore, increased MoSi₂ and TiC content can significantly impede the grain growth of the γ -Ni matrix, resulting in grain refinement of the γ -Ni solid solution and providing strengthening and improved hardness, in line with the Hall–Petch mechanism for strength enhancement [40]. However, the uneven distribution of fan-shaped TiC

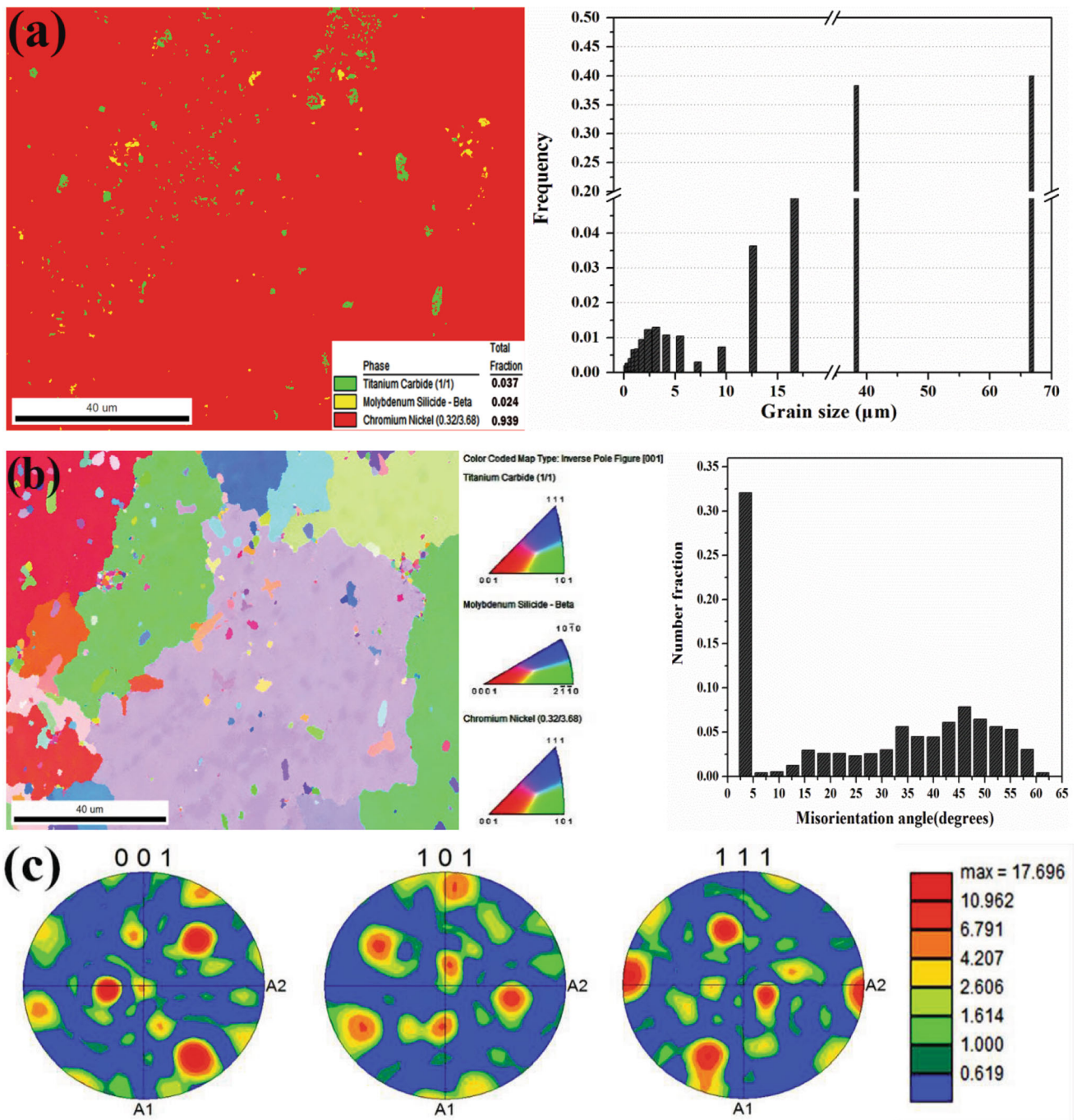


Fig. 6 (a) EBSD phase mapping images (red: γ -Ni, yellow: MoSi_2 , green: TiC) (b) EBSD grain IPFs and misorientation angles, and (c) $\{001\}$, $\{101\}$, and $\{111\}$ PFs of the γ -Ni matrix in the 20NT composite coating.

ceramic reinforcement particles in the 30NT composite coating leads to defects and hardness fluctuations.

The surface indentation morphology illustrates the microhardness of the Ni-based composite coatings with increasing Ti_3SiC_2 content, as depicted in Fig. 8. An uplifting is observed in the 10NT coating due to significant plastic deformation along the diamond-shaped indentation (Fig. 8a). In the case of the 30NT coating, cracks are

generated along the sharp corners of the diamond-shaped indentation because the uneven distribution of segregated MoSi_2 and TiC ceramic reinforcement increases brittleness (Fig. 8c). Although the high hardness and strength of laser in situ generated TiC and MoSi_2 ceramic reinforcement can enhance the mechanical properties of the composite coatings, their inherently low fracture toughness ($2\text{--}3 \text{ MPa m}^{1/2}$) and relatively weak creep strength increase the

likelihood of crack formation [30]. Only the 20NT coating presents an intact indentation surface without macro-defects (Fig. 8b). The 10NT coating is more prone to plastic deformation due to the presence of large coarse γ -Ni dendrites and lower TiC and MoSi₂ content. Conversely, in the 20NT coating, increased TiC and MoSi₂ result in a relatively high elastic modulus and enhanced wear resistance. However, in the 30NT coating, an excess of Ti₃SiC₂ creates a heterogeneous structure with large aggregates of TiC and MoSi₂ ceramic reinforcement, exacerbating crack formation.

As shown in Fig. 9 and Table 3, the 20NT composite coating exhibited higher nanohardness and elastic modulus values compared to the 10NT coating (increasing from 8.27 to 11.76 GPa and from 159.97 to 168.22 GPa, respectively). According to traditional fracture mechanics [41], the improved resistance to cracking of the 20NT composite coating can be primarily attributed to the increased content of laser in situ generated fine TiC and MoSi₂ precipitates.

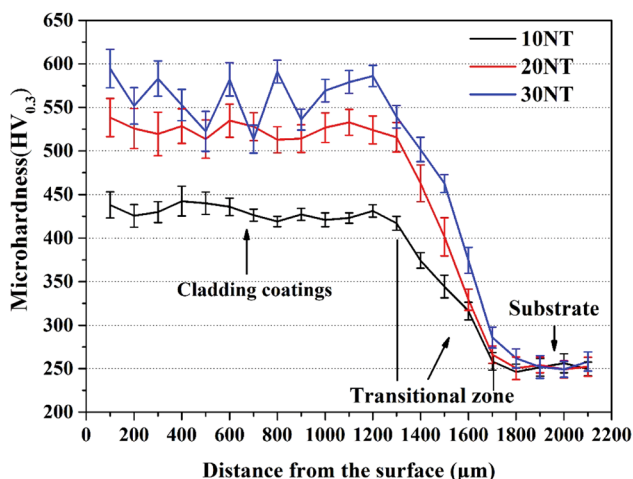


Fig. 7 Microhardness values for composite coatings with various Ti₃SiC₂ contents.

An increased content of fine TiC and MoSi₂ precipitates significantly reduces the mean grain size from 82 to 52.4 μm of the γ -Ni solid solution and further enhances fracture strength through refinement strengthening based on the Hall–Petch relationship [42]. Moreover, the microhardness of the laser clad coatings may be influenced by other factors, such as the residual stress state [11]. Discontinuities were observed in the load-displacement curve of the 30NT composite coating, likely due to the heterogeneous structure caused by the severe segregation of coarse TiC ceramics (Fig. 9a). Notably, in all three prepared composite coatings, the elastic recovery rate and plastic deformation resistance (H^3/E^2) increase with the rising content of in situ generated TiC and MoSi₂ precipitates. To further explore the flexural properties and analyze the fracture mechanism, the fractured surfaces of the flexural test samples were examined by SEM (Figs. 9b and 10). The 20NT composite coating displayed higher flexural strength compared to the 10NT coating (increasing from 1046.58 to 1651.37 MPa) due to the increased content of in situ generated fine TiC and MoSi₂ precipitates, as indicated in Table 3. The fractured surfaces of the 10NT and 20NT composite coatings (Fig. 10a, b) showed evidence of transgranular cleavage, grain extraction, some dimples, and a few micro-cracks. This suggests that the fracture mechanisms for the 10NT and 20NT coatings are characterized by a combination of ductile and brittle fracture [44]. In the case of the 30NT coating, the flexural strength significantly decreased to 406.83 MPa, and numerous micro-cracks and pores were observed (Fig. 10c). The formation of micro-cracks, pores, and the extraction of friable coarse TiC particles negatively impacted the flexural strength of the 30NT composite coating.

Tribological Properties at Elevated Temperatures

Fig. 11 presents the tribological properties, including the mean friction coefficients and wear rates, of the 10NT and

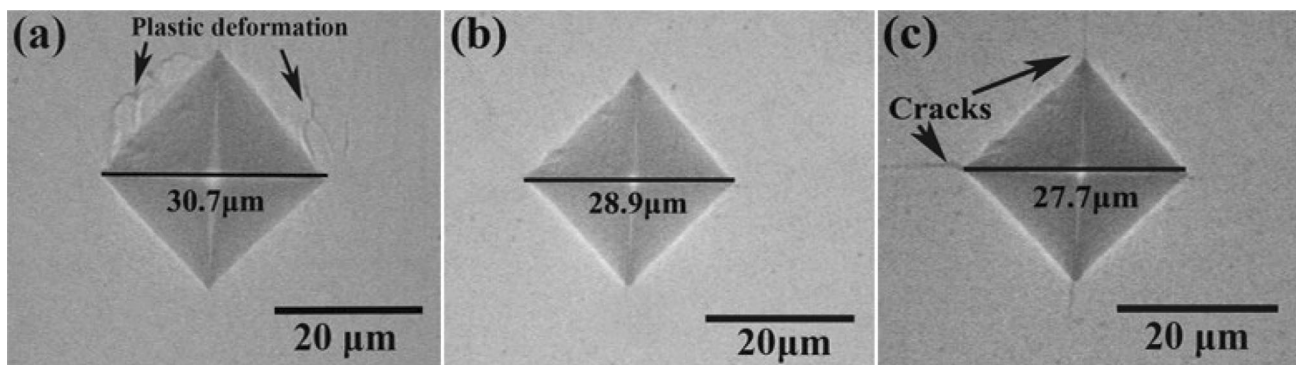


Fig. 8 Surface indentation morphology illustrating the microhardness of the composite coatings: (a) 10NT, (b) 20NT, and (c) 30NT.

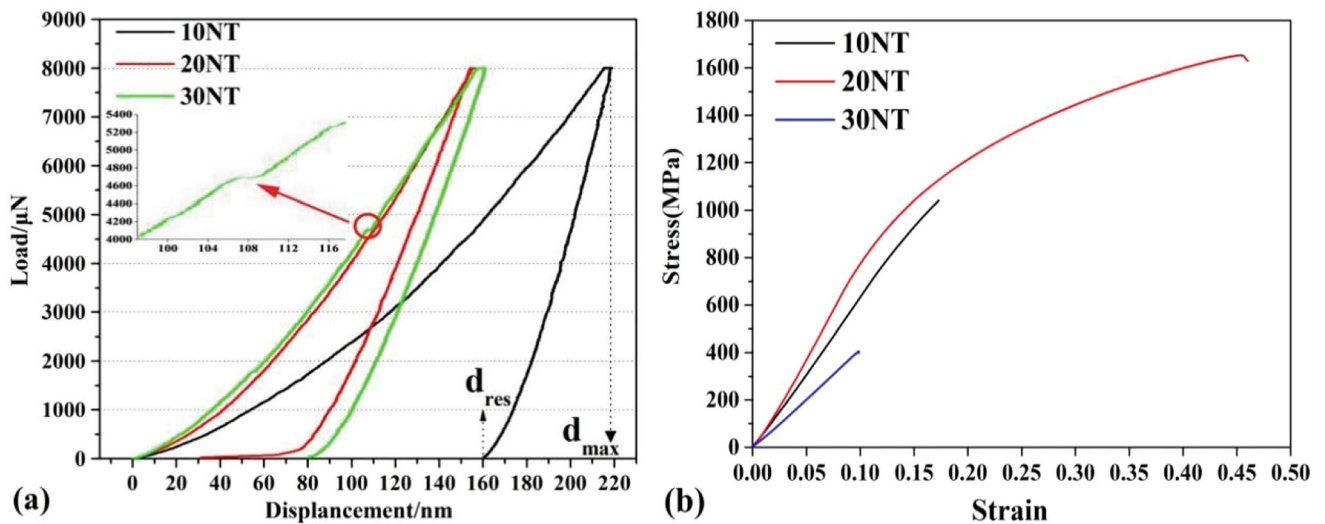


Fig. 9 Nanoindentation (a) and three-point bending test (b) results for Ni-based composite coatings with varying Ti_3SiC_2 content.

Table 3 The mechanical properties of the 10NT, 20NT, and 30NT composite coatings.

Mechanical properties	10NT	20NT	30NT
Hardness, H(GPa)	8.27 ± 0.15	11.76 ± 0.25	16.61 ± 0.31
Elastic modulus, E(GPa)	159.97 ± 1.63	168.22 ± 1.85	174.71 ± 2.74
Elastic strain (H/E)	0.0517	0.0699	0.0951
Elastic recovery (%)	26.99	53.75	50.28
Plastic deformation resistance (H^3/E^2)	0.0221	0.0575	0.1501
Flexural strength (MPa)	1046.58 ± 7.45	1651.37 ± 9.82	406.83 ± 12.93

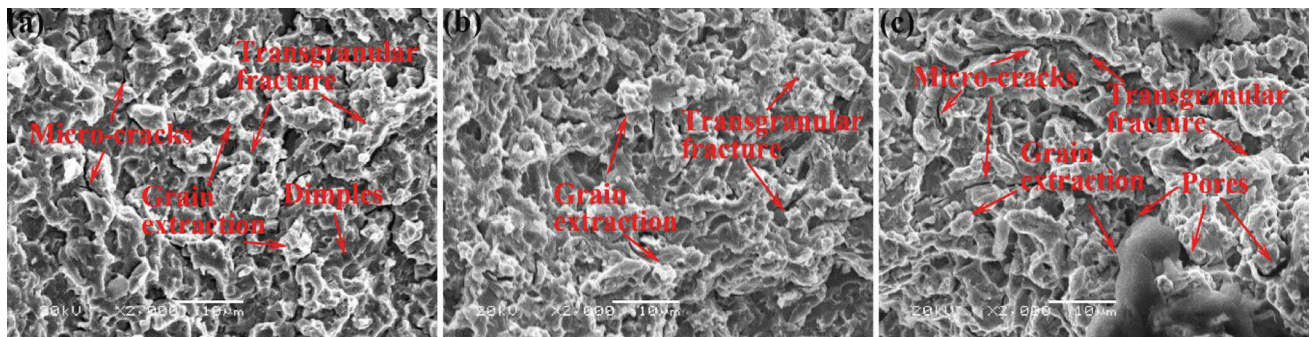


Fig. 10 SEM images of the fractured surface of the composite coatings after flexural tests: (a) 10NT, (b) 20NT, and (c) 30NT.

20NT composite coatings while sliding against Si_3N_4 balls at temperatures ranging from 30 to 1000 °C. Fig. 11a shows that the mean friction coefficient and wear rate of the 10NT coating gradually increase from 30 to 400 °C, reaching maximum values of 0.45 and $3.96 \times 10^{-5} \text{ mm}^3/\text{N m}$ at 400 °C, respectively. Conversely, the mean friction coefficient of the 20NT coating initially increases and then decreases with rising temperature, but its wear rate increases from 3.16 to $3.57 \times 10^{-5} \text{ mm}^3/\text{N m}$ up to 400 °C. From 30 to 400 °C, the tribological performance of the 20NT composite coating significantly outperforms that of the 10NT coating due to its higher content of laser

in situ generated fine TiC and $MoSi_2$ precipitates. When the temperature is further increased from 400 to 800 °C, the wear rates of both the 10NT and 20NT composite coatings exhibit similar trends, with their mean friction coefficients and wear rates decreasing from 0.46 and $3.99 \times 10^{-5} \text{ mm}^3/\text{N m}$ to minimum values of 0.26 and $3.41 \times 10^{-6} \text{ mm}^3/\text{N m}$ for 10NT, and from 0.41 and $3.71 \times 10^{-5} \text{ mm}^3/\text{N m}$ to minimum values of 0.30 and $4.63 \times 10^{-6} \text{ mm}^3/\text{N m}$ for 20NT, respectively. A further increase in temperature up to 1000 °C leads to an additional increase in wear rates. Compared to the pure Hastelloy C276 coating, both the 10NT and 20NT

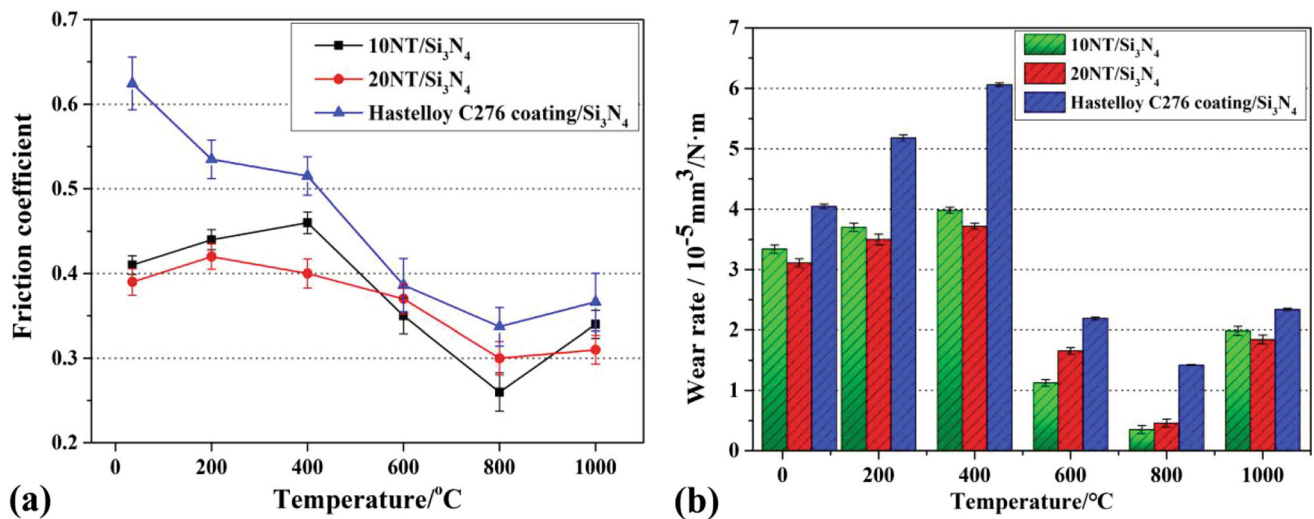


Fig. 11 (a) Mean friction coefficients and (b) wear rates of the composite coatings sliding against Si₃N₄ balls.

composite coatings exhibit significantly improved tribological properties, with reduced mean friction coefficients and wear rates as the temperature rises from 30 to 1000 °C (Fig. 11a, b). Thus, these laser in situ generated TiC and MoSi₂ reinforcing precipitates contribute to enhancing the tribological performance of pure Ni-based alloy coatings.

Fig. 12a, b displays the worn surface characteristics of the 10NT and 20NT composite coatings while sliding against Si₃N₄ balls at 30 °C. The worn surface of the 10NT coating shows significant furrowed scratches and a few micro-cracks, along with numerous flaky debris areas (Fig. 12a). In contrast, the worn surface of the 20NT coating exhibits island-shaped delamination regions and a substantial amount of scattered fine debris (Fig. 12b). The surface appearance of the peeled debris particles mainly consists of large flakes, and the exfoliated debris mainly exists as lamellar particles, indicating that adhesive wear is the dominant wear mechanism for the 10NT coating. Similarly, for the 20NT coating, the worn surface debris and exfoliated debris are coarse particles, suggesting that adhesive wear accompanied by mild oxidative wear is the dominant wear mechanism [43]. As can be seen from the inferred wear models in Fig. 17a, the microstructure of both the 10NT and 20NT composite coatings primarily consists of continuous ductile γ -Ni dendrites. The presence of coarse dendrites in the form of γ -Ni solid solution significantly reduces the overall strength of these coatings, making the ductile regions in the coating more susceptible to wear and tear. The columnar dendrites at the surface lack the strength to resist stamping and deformation, further exacerbating adhesive wear of the coating surface. However, the presence of laser in situ induced TiC and MoSi₂ reinforcement acts as a hard skeleton, contributing to improved wear resistance in these coatings. Because the

ductile γ -Ni dendrites are prone to plastic deformation, the worn surface initially experiences compression and deformation, leading to the formation of several deformed layers originating from primitive micro-cracks at 30 °C [44]. TiC and MoSi₂ reinforcement effectively reduce shear damage caused by the Si₃N₄ ball on the coating surface and enhances the resistance of the γ -Ni alloy matrix to plastic deformation. This results in a significantly reduced wear rate and the formation of an uneven frictional surface in both the 10NT and 20NT composite coatings (Fig. 17a). Compared to the 10NT coating, the 20NT composite coating exhibits enhanced hardness and plastic deformation resistance due to the increased content of laser in situ generated TiC and MoSi₂, leading to improved wear resistance at 30 °C.

As the test temperature increases from 30 to 400 °C, the worn surfaces of the 10NT and 20NT coatings exhibit a significant presence of fine abrasive chips and a few extrusion layers. Simultaneously, the occurrence of black island regions resulting from adhesive shear separation decreases (Fig. 12c, d). When combined with the micrographs of the worn debris shown in Fig. 13b, d, it becomes evident that the abrasive debris is relatively small in size and granular in shape, suggesting that the wear mechanism of both composite coatings is an oxidative wear with mild abrasive wear. As the temperature continues to rise, the two composite coatings become more susceptible to shear damage due to contact between the Si₃N₄ balls and the coating surface, resulting in the maximum wear rate occurring at 400 °C. This outstanding tribological performance can be primarily attributed to the even distribution of laser-induced MoSi₂ and TiC fine particles within the γ -Ni dendrite matrix, in comparison with the pure Hastelloy C276 coating. The formation of MoSi₂ and TiC

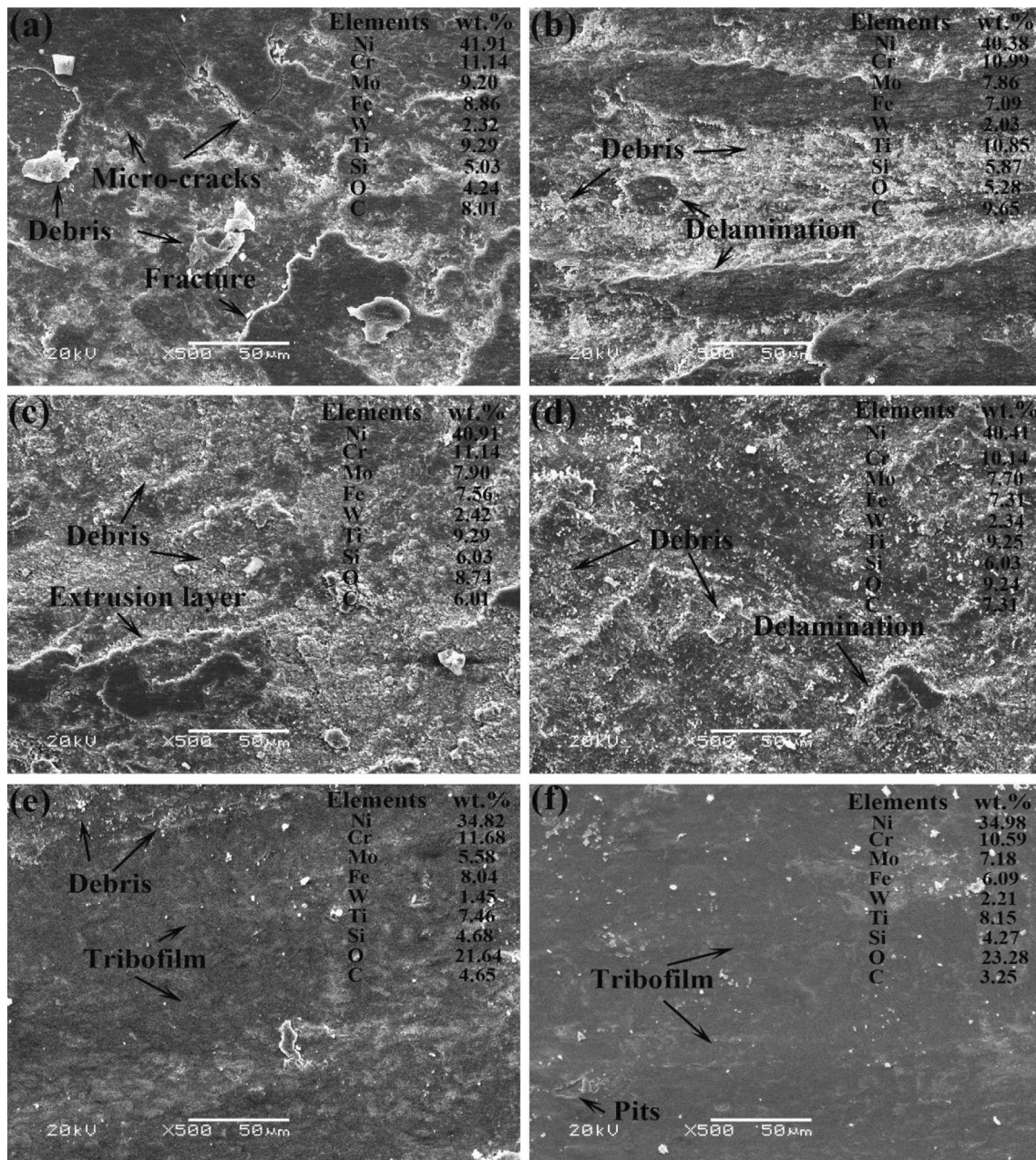


Fig. 12 SEM morphology of the worn surface of the 10NT coating at (a) 30, (c) 400, and 800 °C, and 20NT coating at (b) 30, (d) 400, and (f) 800 °C.

reinforcements effectively counteracts the softening and plastic deformation caused by serious intergranular slip in the pure γ -Ni matrix at elevated temperatures. Raman characterization of the worn surface reveals that, at 400 °C, small amounts of metal oxides are formed in both the 10NT and 20NT coatings (Fig. 15). In the 10NT coating, these oxides mainly consist of Fe_3O_4 and variants (M_3O_4 spinel oxides), along with small amounts of TiO_2 , Cr_2O_3 , and $NiTiO_3$. In the 20NT composite coating, the oxides primarily consist of $NiTiO_3$ and TiO_2 . The freshly exposed surface during wear continues to oxidize as the temperature

reaches 400 °C. Due to the exceptional oxidative resistance of the $MoSi_2$ reinforcement, the resulting oxidative layer is intermittent and tends to be buried within worn debris, as illustrated in Fig. 17b. Consequently, a locally continuous oxidative layer fails to form on the abrasion surface, and exfoliated oxidative particles exacerbate the three-body abrasive wear of the 10NT and 20NT composite coatings [45]. Meanwhile, the γ -Ni matrix starts to soften, leading to a roughened worn surface at 400 °C (Fig. 14c, d). The relatively weak shear strength of loose Fe_3O_4 and variants particles contribute to wear damage during the frictional

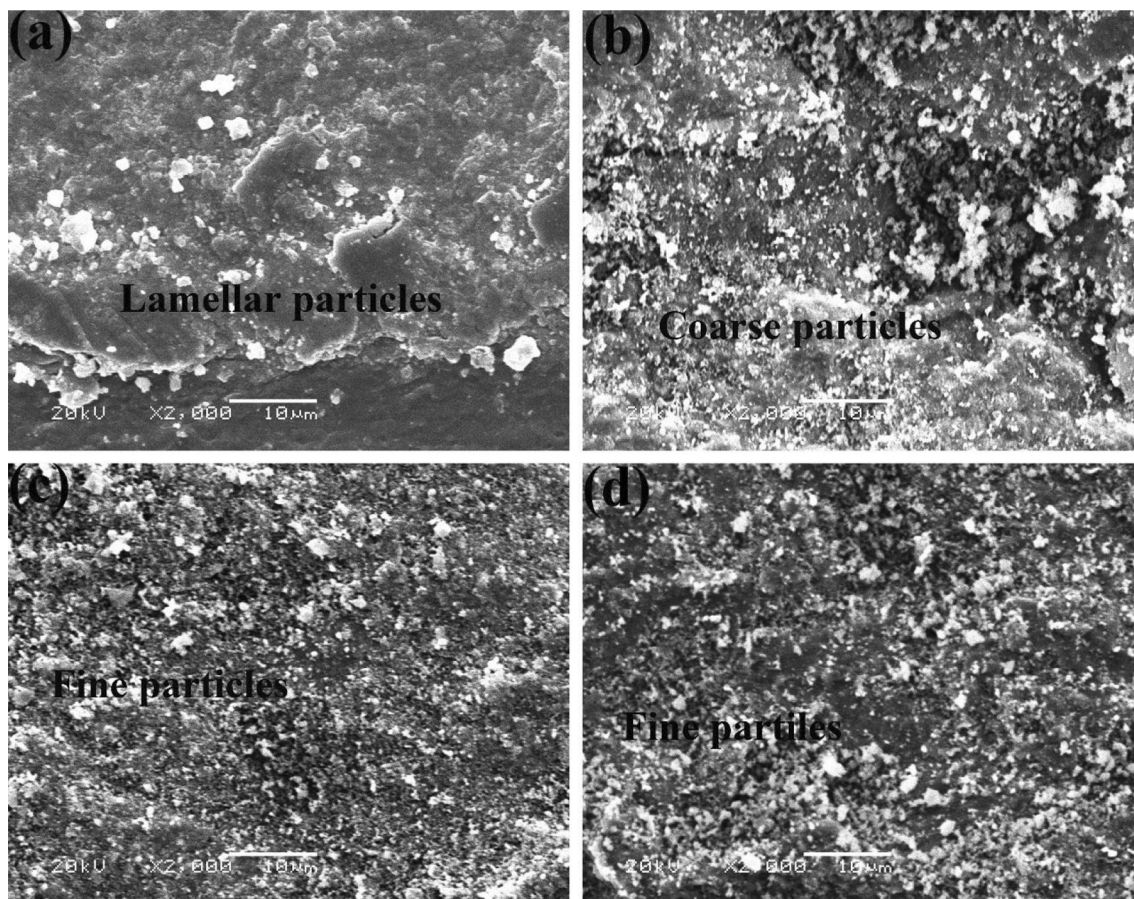


Fig. 13 Micrographs of the wear debris of the 10NT coating at (a) 30 and (c) 400 °C, and of the 20NT coating at (b) 30 and (d) 400 °C.

shear process [46]. Consequently, the 10NT coating exhibits a higher friction coefficient and wear rate than the 20NT composite coating at 400 °C.

For both composite coatings, when the test temperature rises to 800 °C, the worn surface appears relatively smooth, accompanied by a continuous compact frictional layer and a few parallel scratches (Fig. 12e, f). Compared to the three-dimensional morphology of the worn surface at 30 and 400 °C, there is a noticeable absence of small debris and adherent shear layers at 800 °C, resulting in effectively reduced surface roughness (Fig. 14a–f). Meanwhile, the depth and width of the worn surface reach their minimum values at this temperature. Based in Fig. 15, it would seem that NiTiO_3 and (especially in the 20NT coating) NiMoO_4 are the dominant phases, while it is the other metal oxides that exist in smaller amounts, such as Ti_3O_5 , MoO_2 , and TiO_2 , are formed on the worn surface of the 10NT coating and 20NT composite coating. Compared to the Raman results at 30 and 400 °C, the results at 800 °C reveal a significant increase in the variety and relative content of formed oxides, suggesting that the smooth continuous lubricating films consist of NiTiO_3 and NiMoO_4 complex and a small amount of other metal oxides. As the

temperature reaches 800 °C, the intermittent in situ TiC and MoSi_2 reinforcements are oxidized due to the rising test temperature and accumulated frictional heat. Consequently, a dynamic equilibrium between the production and removal of oxidative lubricating tribofilms is gradually established, resulting in a continuous and smooth oxidative layer covering a large area, as depicted in Fig. 17c. This continuous and smooth lubricating oxidative film contributes to preventing direct shear contact from the Si_3N_4 balls, thereby providing excellent wear resistance and lubrication for the composite coating [47].

Fig. 16 presents SEM micrographs of the worn surface and EDS mapping images of the 10NT and 20NT composite coatings at 1000 °C. The previously established successive and smooth lubricating films at 800 °C are now disrupted, resulting in noticeable cutting and spalling and a significant increase in the mean friction coefficient and wear rate (Fig. 16). Particularly, there is a notable change in the relative Si and O content. The decrease in O element concentration in the 10NT (from 21.64 to 16.92 wt.%) and 20NT (from 23.28 to 15.71 wt.%) coatings can mainly be attributed to the detachment of complete and continuous oxide films as the test temperature increases from 800 to

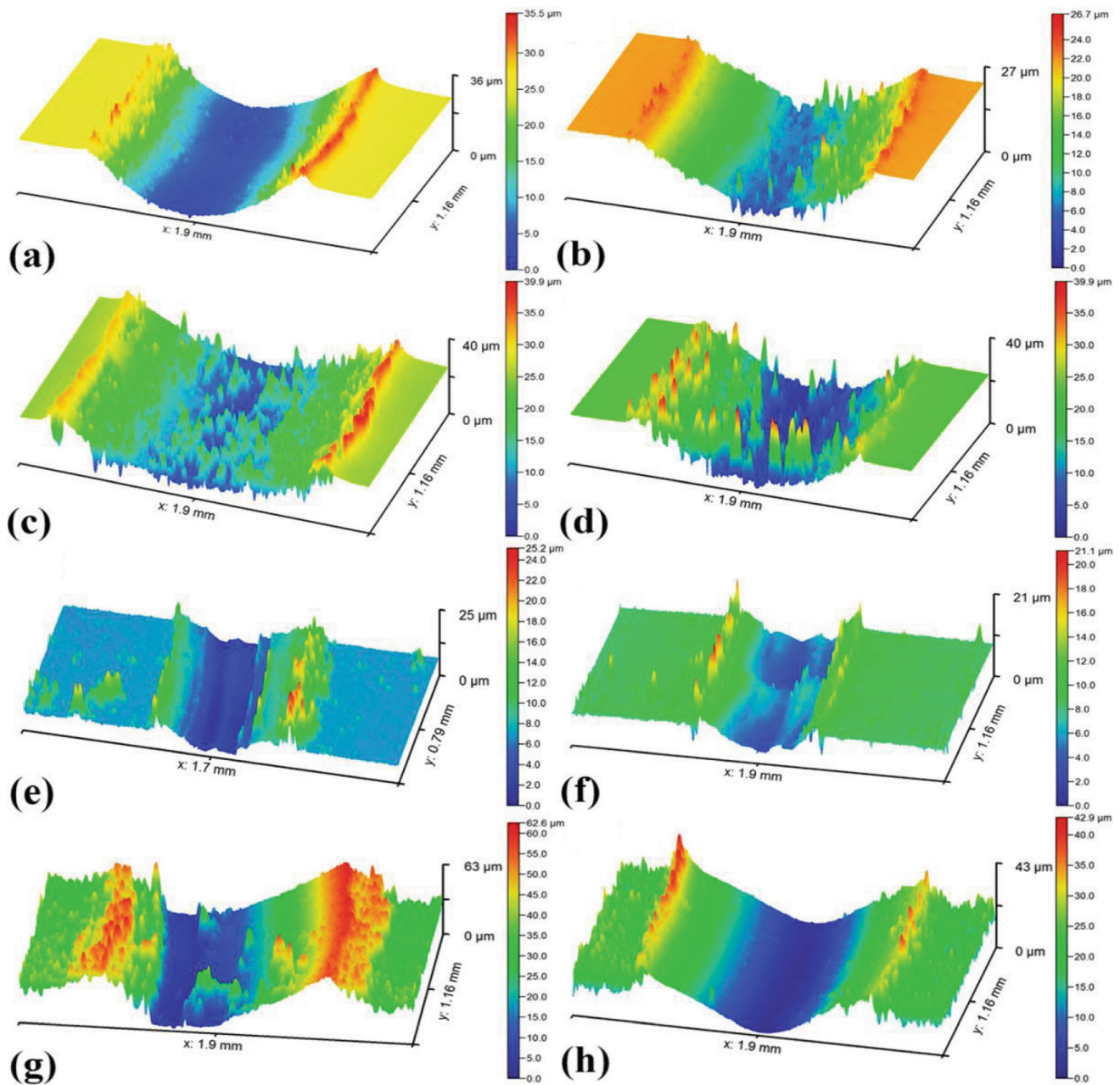


Fig. 14 Three-dimensional morphology of the worn surface of the 10NT coating at (a) 30, (c) 400, (e) 800, and (g) 1000 °C, and the 20NT coating at (b) 30, (d) 400, (f) 800, and (h) 1000 °C.

1000 °C. Conversely, the increase in Si content in the 10NT (from 4.68 to 12.29 wt.%) and 20NT (from 4.27 to 10.30 wt.%) coatings indicates that Si from the Si_3N_4 mating ball is transferred to the worn surface of the composite coating during the sliding process, resulting in enrichment of this element and adhesive wear as the test temperature reaches 1000 °C. Compared to the 10NT coating, the 20NT composite coating exhibits significantly fewer adherent wear debris, a more uniform distribution of Si and O elements, and less damage to the oxide film (Fig. 16b). Therefore, a smoother and more continuous

lubricating layer is presented, resulting in a lower mean friction coefficient and wear rate for the 20NT composite coating at 1000 °C (Fig. 16).

As the temperature increases to 1000 °C, a considerable amount of NiTiO_3 , MoO_2 , TiO_2 , and NiMoO_4 complex is found on the surface of both worn composite coatings. The significant increase in the NiMoO_4 complex peak intensity on the worn 20NT coating surface indicates a relatively higher NiMoO_4 content in this coating compared to the 10NT coating. The formation and homogeneous distribution of these in situ generated oxides and complexes

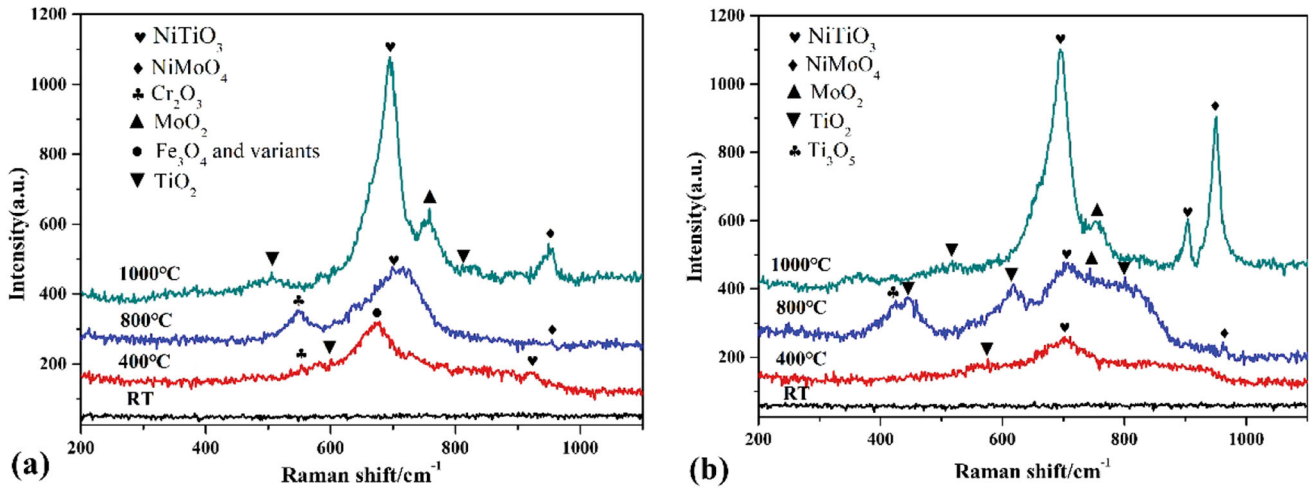


Fig. 15 Typical Raman spectra of worn surfaces of the composite coatings tested at different temperatures: (a) 10NT and (b) 20NT.

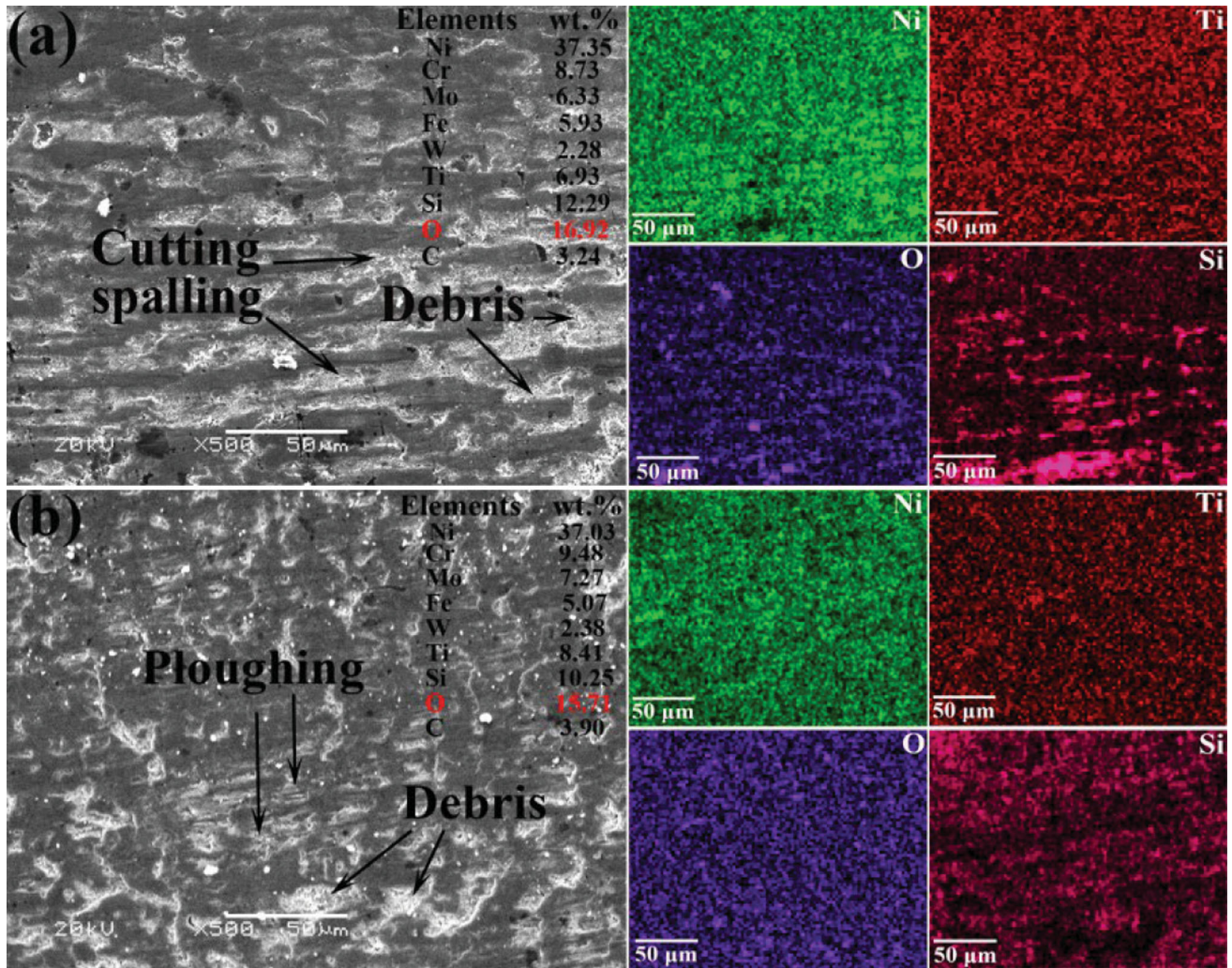
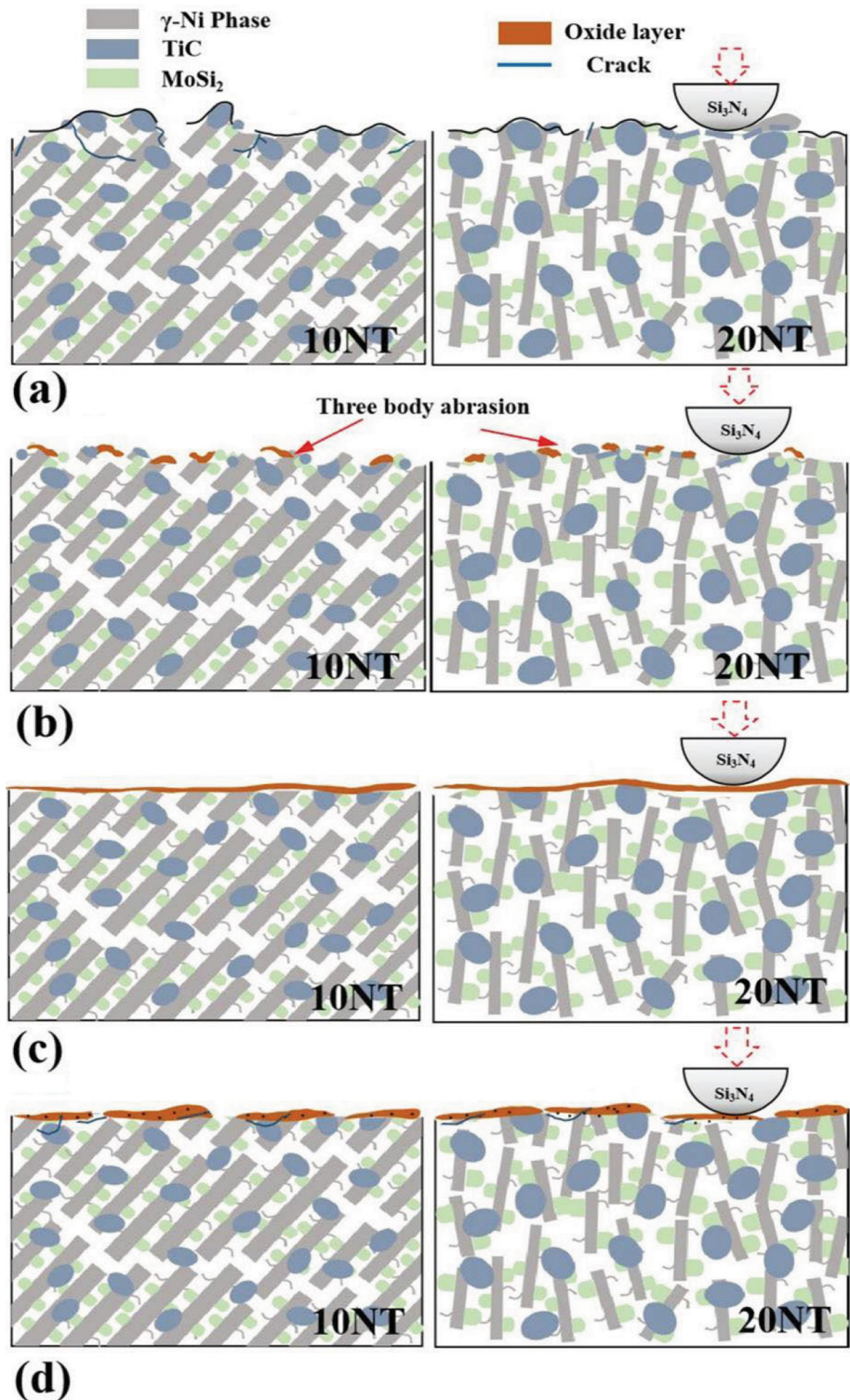


Fig. 16 SEM micrographs of the worn surface and EDS mapping image of the composite coatings at 1000 °C: (a) 10NT and (b) 20NT.

facilitate the creation of continuous lubricating films. Conversely, macro-cracks and fatigue delamination on the worn surface result from surface softening and the formation of dense nanoscale pores in the rigid oxidative tribofilms during the wear process. Consequently, the disrupted oxidative tribofilms reduce the shielding

efficiency of the lubricating layer and increase shear damage, as depicted in Fig. 17d. Simultaneously, the wear mechanism due to contact with Si_3N_4 balls tends to favor adhesive wear during continuous shear, leading to an increase in the friction coefficient and wear rate as the experimental temperature rises to 1000 °C. Meanwhile,

Fig. 17 Schematic illustration of inferred wear models of the 10NT and 20NT composite coatings at various temperatures: (a) 30, (b) 400, (c) 800, and (d) 1000 °C.



extruded accumulation layers are distributed on both worn sides of the 10NT and 20NT composite coatings due to the continuous ductile γ -Ni dendrite matrix being more susceptible to plastic deformation and continuous shear extrusion at 1000 °C (Fig. 14 g, h). The presence of a higher content of NiMoO₄ complex on the worn surface contributes to reducing the extent of shear damage to the lubricating film, resulting in the improved tribological performance of the 20NT composite coating at 1000 °C.

Conclusions

1. Ni-based composite coatings with varying Ti₃SiC₂ content were applied to the surface of Inconel 718 alloy using laser in situ synthesis technology. As the Ti₃SiC₂ content increased, these prepared composite coatings included the γ -Ni matrix and an increased amount of laser in situ generated TiC and MoSi₂ reinforcement.
2. At Ti₃SiC₂ contents of 10 and 20 wt.%, the microstructure of the composite coatings was characterized by coarse γ -Ni dendrites, slender MoSi₂ interdendritic phases, and fine TiC ellipsoidal particles. The appropriate content of laser in situ induced TiC and MoSi₂ reinforcing precipitates significantly hindered the orientation growth and inhibited grain growth in the γ -Ni matrix. However, an excess of Ti₃SiC₂ (30 wt.%) led to the formation of clusters of TiC particles and the occurrence of severe defects.
3. The Ni-based composite coating with 20 wt.% Ti₃SiC₂ exhibited relatively superior mechanical properties and lower mean friction coefficients and wear rates compared to the Ni-based composite coating with 10 wt.% Ti₃SiC₂, owing to the increased volume fraction of laser in situ generated fine TiC and MoSi₂ precipitates.
4. The prepared Ni-based composite coatings with 10 and 20 wt.% Ti₃SiC₂ exhibited a reduce of the friction coefficient and wear rate compared to the pure Hastelloy C276 coating because laser in situ induced TiC and MoSi₂ reinforcements helped to reduce the cutting stress and resist plastic deformation from 30 to 400 °C. Furthermore, the prepared coatings could form continuous, smooth oxide layers to shield the coating from shear damage at 800 °C. However, when the temperature was increased to 1000 °C, the breaking of these continuous lubricating films resulted in noticeable cutting and spalling and limited their protective capabilities. The presence of NiMoO₄ in the composite coating with 20 wt.% Ti₃SiC₂ contributed to reducing the destruction of the lubricating film, resulting in improved tribological performance.

Acknowledgments This work was supported by the Inner Mongolia Science and Technology Program (Grant No. 2020GG0313), the Innovative Research Team in Universities of Inner Mongolia Autonomous Region (Grant No. NMGIRT2211), Inner Mongolia University of Technology Key Discipline Team Project of Materials Science (Grant No. ZD202012), the Inner Mongolia Natural Science Foundation (Grant No. 2022QN05030, 2022QN05025 and 2022QN05005), the Basic Scientific Research Expenses Program of Universities directly under Inner Mongolia Autonomous Region (Grant No. JY20220123) and the Natural Science Foundation of Inner Mongolia University of Technology (Grant No. ZZ202105).

Author contributions SC was contributed to project administration, writing—review and editing, conceptualization, funding acquisition, supervision. PZ was contributed to methodology, writing—original draft, software. SF was contributed to investigation, methodology. JZ was contributed to conceptualization, validation, investigation, project administration.

Declarations

Conflict of interest All authors declare that they have no known competing financial interests or personal relationships that could have appeared to influence the work reported in this paper.

References

1. I.G. Akande, O.O. Oluwole and O.S. Fayomi, Overview of Mechanical, Microstructural, Oxidation Properties and High-Temperature Applications of Superalloys, *Mater Today Proc*, 2021, **43**, p 2222–2231.
2. G.H. Cao, T.Y. Sun and C.H. Wang, Investigations of γ' , γ'' and δ Precipitates in Heat-Treated Inconel718 Alloy Fabricated by Selective Laser Melting, *Mater Charact*, 2018, **136**, p 398–406.
3. B.S. Yilbas and H. Ali, Laser Texturing of Hastelloy C276 Alloy Surface for Improved Hydrophobicity and Friction Coefficient, *Opt. Laser Eng.*, 2016, **78**, p 140–147.
4. Y.H. Kong, L. Wang and Z.J. Yin, The Microstructures and Anti-Corrosion Behavior of the Thermal Sprayed Hastelloy C276 Coating on Substrate of Q235 Steel, *Mater. Res. Express.*, 2019, **6**(26), p 571–584.
5. C.P. Mulligan, R. Wei and G. Yang, Microstructure and Age Hardening of C276 Alloy Coatings, *Surf. Coat. Technol.*, 2015, **270**(10), p 299–304.
6. T. Rong, D.D. Gu, Q.M. Shi, S.N. Cao and M.J. Xia, Effects of Tailored Gradient Interface on Wear Properties of WC/Inconel 718 Composites Using Selective Laser Melting, *Surf. Coat. Technol.*, 2016, **307**, p 418–427.
7. L.Y. Fang, H. Yan, Y.S. Yao, P.L. Zhang and Q.S. Gao, Reactive Fabrication and Effect of NbC on Microstructure and Tribological Properties of CrS Co-Based Self-Lubricating Coatings by Laser Cladding, *Materials*, 2018, **11**, p 44.
8. Y.C. Zhang, Z.G. Li and P.L. Nie, Carbide and Nitride Precipitation During Laser Cladding of Inconel 718 Alloy Coating, *Opt. Laser Technol.*, 2013, **52**, p 30–36.
9. H. Yan, K.W. Liu, P.L. Zhang and J. Zhao, Fabrication and Tribological Behaviors of Ti₃SiC₂/Ti₅Si₃/TiC/Ni-Based Composite Coatings by Laser Cladding for Self-Lubricating Applications, *Opt. Laser Technol.*, 2020, **126**, 106077.
10. Y. Zhu, X.B. Liu, Y.F. Liu and G. Wang, Development and Characterization of Co-Cu/Ti₃SiC₂ self-Lubricating Wear Resistant Composite Coatings on Ti6Al4V Alloy by Laser Cladding, *Surf. Coat. Technol.*, 2021, **424**, 127664.

11. S.S. Lu, J.S. Zhou, L.Q. Wang and J. Liang, Influence of MoSi₂ on the Microstructure and Elevated-Temperature Wear Properties of Inconel 718 Coating Fabricated by Laser Cladding, *Surf. Coat. Technol.*, 2021, **424**, 127665.
12. I. Tudela, A.J. Cobley, and Y. Zhang, Tribological Performance of Novel Nickel-Based Composite Coatings with Lubricant Particles, *Friction*, 2018, 7(2), p 16980.
13. J.M. Zhen, J. Cheng, H. Tan, S.Y. Zhu and J. Yang, Investigation of Tribological Characteristics of Nickel Alloy-Based Solid-Lubricating Composites at Elevated Temperatures Under Vacuum, *Friction*, 2021, 9(5), p 990–1001.
14. G. Bolelli, A. Candeli, L. Lusvardi and A. Ravoux, Tribology of NiCrAlY+Al₂O₃ Composite Coatings by Plasma Spraying with Hybrid Feeding of Dry Powder+Suspension, *Wear*, 2015, **344**(345), p 69–85.
15. Q.S. Gao, H. Yan, Y.Q. Qin, P.L. Zhang, J.L. Guo and Z.F. Chen, Laser Cladding Ti-Ni/TiN/TiW+TiS/WS₂ Self-Lubricating Wear Resistant Composite Coating on Ti-6Al-4V alloy, *Opt. Laser Technol.*, 2019, **113**, p 182–191.
16. B. Li, Y.M. Gao, C. Li, and F. Liu, Improved tribological performance of Nickel Based High Temperature Lubricating Composites with Addition of Metallic Oxides. *Wear*, 2021, 480(481), p 203938.
17. J. Cheng, Y. Yu, L.C. Fu, F. Li, Z.H. Qiao and J.S. Li, Effect of TiB₂ on Drysliding Tribological Properties of TiAl Intermetallic, *Tribol. Int.*, 2013, **62**, p 91–99.
18. V. Testa, S. Morelli, G. Bolelli, L. Lusvardi and S. Joshi, Micromechanical Behaviour and Wear Resistance of Hybrid Plasma-Sprayed TiC Reinforced Tribaloy-400, *Surf. Coat. Technol.*, 2021, **430**, 127682.
19. S. Banthia, S. Sengupta and S. Das, Cu, Cu-SiC Functionally Graded Coating for Protection Against Corrosion and Wear, *Surf. Coat. Technol.*, 2019, **374**, p 833–844.
20. A. Khorram, A.D. Jamaloei, M. Paidar and X.J. Cao, Laser Cladding of Inconel 718 with 75Cr₃C₂+30(80Ni20Cr) Powder: Statistical Modeling and Optimization, *Surf. Coat. Technol.*, 2019, **378**, 124933.
21. H.Z. Moghaddam, M. Sharifitabar and G. Roudini, Microstructure and Wear Properties of Fe-TiC Composite Coatings Produced by Submerged arc Cladding Process Using Ferroalloy Powder Mixtures, *Surf. Coat. Technol.*, 2019, **361**, p 91–101.
22. J. Sun, T. Li and G.P. Zhang, Effect of Thermodynamically Metastable Components on Mechanical and Oxidation Properties of the Thermal-Sprayed MoSi₂ Based Composite Coating, *Corros. Sci.*, 2019, **155**, p 146–154.
23. L. Sun and J. Pan, Fabrication and Characterization of TiC Particle Reinforced MoSi₂ Composites, *J. Eur. Ceram. Soc.*, 2002, **22**, p 791–796.
24. J. Xu, W.J. Liu and M.L. Zhong, Microstructure and Dry-Sliding Wear Behavior of MoS₂/TiC/Ni Composite Coatings Prepared by Laser Cladding, *Surf. Coat. Technol.*, 2006, **200**, p 4227–4232.
25. Z.C. Feng, Y.F. Liu, Li Y, G.B. Sun, Z. Zhang, and C.X. Shi, a Microstructure and High Temperature Reciprocating Sliding Wear Properties of MoSi₂/TiC/γ-Ni Composite Coating In-Situ Synthesized by Co-Axial Powder Feeding Plasma Transferred arc Cladding, *Tribol. Int.*, 2019, 129, p 82-91.
26. B.B. Xin, Y.J. Yu and J.S. Zhou, Effect of Copper Molybdate on the Lubricating Properties of NiCrAlY Laser Clad Coating at Elevated Temperatures, *Surf. Coat. Technol.*, 2017, **313**, p 328–336.
27. H. Yu, W. Zhang, H. Wang, X. Ji, Z. Song and X. Li, In-situ Synthesis of TiC/Ti Composite Coating by High Frequency Induction Cladding, *J. Alloys Compd.*, 2017, **701**, p 244–305.
28. N. Durlu, Titanium Carbide-Based Composites for High Temperature Applications, *J. Eur. Ceram. Soc.*, 1999, **19**, p 2415–2419.
29. Y.F. Liu, S.G. Zhuang and X.B. Liu, Microstructure Evolution and High-Temperature Tribological Behavior of Ti₃SiC₂ Reinforced Ni60 Composite Coatings on 304 Stainless Steel by Laser Cladding, *Surf. Coat. Technol.*, 2021, **420**, 127335.
30. H. Torres, M.R. Ripoll and B. Prakash, Tribological Behavior of Self-Lubricating Materials at high Temperatures, *Int. Mater. Rev.*, 2018, **63**(5), p 309–340.
31. L. Kong, S. Zhu, and Z. Qiao, Effect of Mo and Ag on the Friction and wear Behavior of ZrO₂(Y₂O₃)-Ag-CaF₂-Mo Composites from 20 °C to 1000 °C, *Tribol. Int.*, 2014, 78, p 7-13.
32. M. Niu, Q. Bi and J. Yang, Tribological Performance of a Ni3Al Matrix Self-Lubricating Composite Coating Tested from 30 to 1000 °C, *Surf. Coat. Technol.*, 2012, **206**, p 3938–3943.
33. S.Y. Zhu, J. Cheng, Z.H. Qiao and J. Yang, High Temperature Solid-Lubricating Materials: a Review, *Tribol. Int.*, 2019, **133**, p 206–233.
34. B.B. Xin, Y.J. Yu and J.S. Zhou, Effect of Silver Vanadate on the Lubricating Properties of NiCrAlY Laser Cladding Coating at Elevated Temperatures, *Surf. Coat. Technol.*, 2016, **307**, p 136–145.
35. W.T. Dang, S.F. Ren and J.S. Zhou, Influence of Cu on the Mechanical and Tribological Properties of Ti₃SiC₂, *Ceram. Int.*, 2016, **42**, p 9972–9980.
36. V. Pasumarthi, Y. Chen, S.R. Bakshi and A. Agarwal, Reaction Synthesis of Ti₃SiC₂ Phase in Plasma Sprayed Coating, *J. Alloys Compd.*, 2009, **484**, p 113–117.
37. A. Takeuchi and A. Inoue, Classification of Bulk Metallic Glasses by Atomic Size Difference, Heat of Mixing and Period of Constituent Elements and its Application to Characterization of the Main Alloying Element, *Mater. Trans.*, 2005, **46**(12), p 2817–2829.
38. S. Pauly, L. Löber, R. Petters, M. Stoica and S. Scudino, Processing Metallic Glasses by Selective Laser Melting, *Mater. Today*, 2013, **16**(1), p 37–41.
39. X. Cai, L. Zhong and Y. Xu, Microstructural Characterization of a V₂C and V₈C₇ Ceramic-Reinforced Fe Substrate Surface Compound Layer by EBSD and TEM, *J. Alloy. Compd.*, 2018, **74**, p 8–20.
40. A. Sanaty-Zadeh, Comparison Between Current Models for the Strength of Particulate-Reinforced Metal Matrix Nanocomposites with Emphasis on Consideration of Hall-Petch Effect, *Mater. Sci. Eng. A*, 2012, **531**, p 112–118.
41. H. Liu, X.J. Li, J. Liu and W.P. Gao, Microstructural Evolution and Properties of dual-layer CoCrFeMnTi_{0.2} High-Entropy Alloy Coating Fabricated by Laser Cladding, *Opt. Laser Technol.*, 2021, **134**, p 106646.
42. Z.K. Fu, H.H. Ding, W.J. Wang, Q.Y. Liu and J. Guo, Investigation on Microstructure and wear Characteristic of Laser Cladding Fe-Based Alloy on Wheel/Rail Materials, *Wear*, 2015, **330–331**, p 592–599.
43. Q. Liu, Y. Bai, H.D. Wang, G.Z. Ma and C.Y. Chu, Microstructural Evolution of Carbides and its Effect on Tribological Properties of SAPS or HVOF Sprayed NiCr-Cr₃C₂ Coatings, *J. Alloys Compd.*, 2019, **803**, p 730–741.
44. J. Joseph, N. Haghdadi, K. Shamlaye, P. Hodgson and M. Barnett, The Sliding Wear Behaviour of CoCrFeMnNi and Alx-CoCrFeNi High Entropy Alloys at Elevated Temperatures, *Wear*, 2019, **428**, p 32–44.
45. Y. Wang, X.B. Liu, Y.F. Liu, Y.S. Luo and Y. Meng, Microstructure and Tribological Performance of Ni60-Based Composite Coatings on Ti6Al4V Alloy with Different Ti₃SiC₂

- Ceramic Additions by Laser Cladding, *Ceram. Int.*, 2020, **46**, p 28996–29010.
46. H. Liu, Q. Gao, J.B. Dai, P.J. Chen, W.P. Gao, J.B. Hao and H.F. Yang, Microstructure and High-Temperature Wear Behavior of CoCrFeNiW_x High-Entropy Alloy Coatings Fabricated by Laser Cladding, *Tribol. Int.*, 2022, **172**, 107574.
47. Y. Zhao, K. Feng, C.W. Yao, P.L. Nie, J. Huang and Z.G. Li, Microstructure and Tribological Properties of laser Cladded Self-Lubricating Nickel-Base Composite Coatings Containing Nano-Cu and h-BN Solid Lubricants, *Surf. Coat. Technol.*, 2019, **359**, p 485–494.

Publisher's Note Springer Nature remains neutral with regard to jurisdictional claims in published maps and institutional affiliations.

Springer Nature or its licensor (e.g. a society or other partner) holds exclusive rights to this article under a publishing agreement with the author(s) or other rightsholder(s); author self-archiving of the accepted manuscript version of this article is solely governed by the terms of such publishing agreement and applicable law.